Spring 4-13-2022

Zero-Power AC Current Sensor

Omar Aragonez
University of New Mexico

Omar Aragonez

Candidate

Mechanical Engineering Department

Department

This thesis is approved, and it is acceptable in quality and form for publication:

Approved by the Thesis Committee:

Dr. Nathan Jackson , Chairperson

Dr. Matthias Pleil

Dr. Fernando Moreu

ZERO-POWER AC CURRENT SENSOR

by

OMAR ARAGONEZ

BACHELOR OF SCIENCE IN MECHANICAL ENGINEERING

THESIS

Submitted in Partial Fulfillment of the
Requirements for the Degree of

Master of Science in Mechanical Engineering

The University of New Mexico
Albuquerque, New Mexico

May 2022

ACKNOWLEDGMENTS

I heartily acknowledge Dr. Nathan Jackson, my advisor and chair of my committee, for always encouraging me during classroom lectures and lab teachings. His advice helped me achieve more than I could have imagined, and now I hold myself to a higher standard as a result of it.

Dr. Matthias Pleil, thank you for introducing me to microelectromechanical systems and for all your help over the years. I'd also like to thank Dr. Fernando Moreu for his insightful comments and suggestions on this work. Gratitude is extended to New Mexico's Established Program to Stimulate Competitive Research (EPSCoR) and to the Consortium of Hybrid Resilient Energy Systems (CHRES) for the funding to pursue this research.

ZERO-POWER AC CURRENT SENSOR

By

Omar Aragonez

Bachelor of Science in Mechanical Engineering, University of New Mexico, 2020

Master of Science in Mechanical Engineering, University of New Mexico, 2022

ABSTRACT

In this study, a magnetic piezoelectric cantilever powered AC current and frequency sensor is proposed. This paper covers the configuration of the experimental setup, finite element modeling of the magnetic coupling, and the optimal spatial location of the magnetic proof mass in relation to the wire for smart grid applications. Solid and stranded copper wires of various gauges were used and carried current up to 30A. The magnets act as a proof mass to lower the frequency while also coupling to the magnetic field generated by the current carrying wire. The frequency of the AC current produces a sinusoidal force on the piezoelectric cantilever. Vibrational energy is then converted to electrical energy which can be used to power a wireless sensor node. Two different cantilevers with varying stiffness are considered as possible power/sensing elements in the proposed sensor. They are tuned to resonate at 60 Hz using neodymium (NdFeB) magnets.

TABLE OF CONTENTS

LIST OF FIGURES

Chapter 1:

Chapter 2:

Chapter 3:

Chapter 4:

Chapter 5:

LIST OF TABLES

Chapter 2:

Chapter 3:

Chapter 4:

NOMENCLATURE

B	Magnetic Flux Density
μ_o	Permeability of Free Space
I_{in}	Current Enclosed
l	Length
I	Current
r	Radial Distance
F	Force Produced by Magnetic Field
N	Newton
Ω	Ohm Electrical Resistance
V	Volt
V_{pp}	Peak to Peak Voltage
W	Watt
T	Tesla
m	Dipole Moment
V	Volume of Magnet
M	Remanence
F_x	Lateral Force Component
F_y	Vertical Force Component
F_z	Longitudinal Force Component
τ_m	Magnetic Torque
m	Meter
B_x	Lateral Component of Magnetic Field

B_y	Vertical Component of Magnetic Field
τ_{F_x}	Torque Produced by Lateral Force
τ_{F_y}	Torque Produced by Vertical Force
τ	Net Torque
Hz	Hertz
l_m	Length of Magnet
t_m	Thickness of Magnet
θ	Magnet Placement Angle
H	Magnetic Intensity
J	Free Current Density
D	Electric Flux Density
E	Electric Field Strength
ρ_e	Volume Density of Free Electric Charges

Chapter 1: Introduction

1.1 Motivation

The technology we use today relies heavily on the information or data gathered from the environment to function properly. The information is gathered from the systems surroundings with sensors and transducers. The concept of a network of physical objects that utilize sensors that connect and exchange data with other devices is known as the Internet of Things (IoT). One of the applications of IoT is the Smart Grid which unlike conventional grids, can provide information as well as deliver power to consumers.

These Smart Grids also rely on sensors to convey information about consumers, transmission lines, and distribution substations (Ghasempour, 2019). Smart Grids and other IoT systems utilize Wireless Sensor Nodes (WSN) to collect and transmit data. WSN's are sensor nodes that can communicate wirelessly via radio modules. Powering these wireless sensors is a crucial step in making smart grids more efficient and sustainable. WSN's and other low-power devices are typically powered by a battery and require regular maintenance where accessibility can be difficult in some cases. A self-sufficient system can reduce cost and save time in these applications. The magnetic field produced by current carrying wires often goes unutilized and is the solution to a zero-power sensor.

A zero-power AC current sensor will be developed and characterized in this thesis. Design parameters of interest will be optimized for this specific application. Parameters to be considered are the spatial location of the sensor, mechanical properties of the sensing element, and effects from different conductor configurations.

1.1.1 Smart Grids

The U.S. power grid and the electric power system that supply the electricity have been serving the country for over 5 decades. Recent advances in these systems are aimed towards decentralizing and automating the grid. Decentralizing the power grid is important to national security and the overall well-being of the community that utilizes it. The reduction of our current dependence on fossil fuel like oil and coal is also of interest. One way to aid the advancement of these goals is to implement a next-generation type of electrical grid known as a smart grid (Bari et al., 2014). Fig. (1.1) below depicts how the various components of a smart grid communicate with one another.

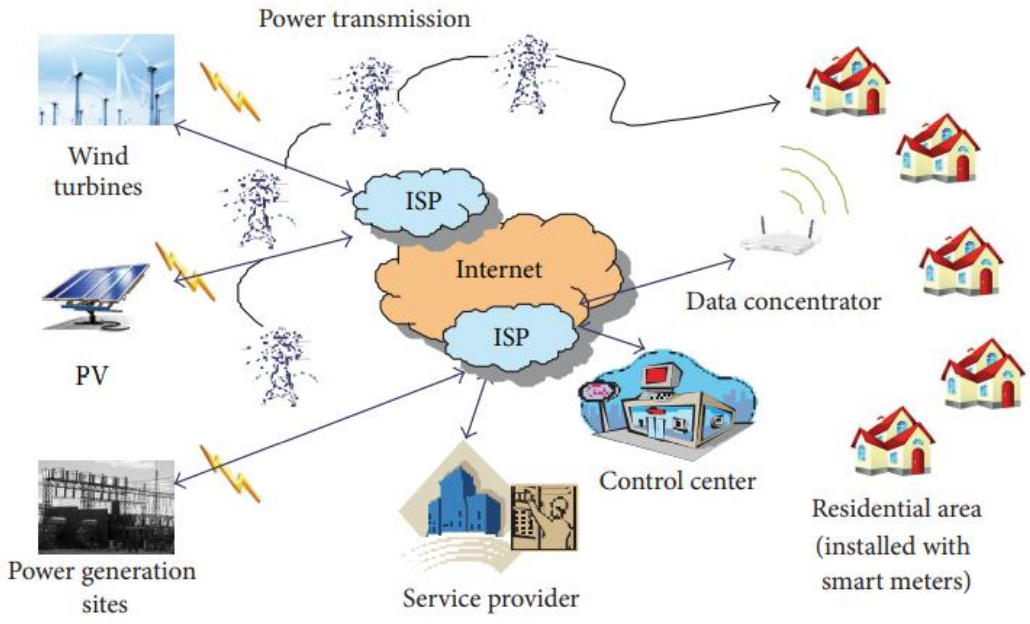

Figure 1. 1: Communication Architecture in a Smart Grid (Bari et al., 2014)

A smart grid is a modern electrical system that utilizes sensors and computers to communicate with the utility. If implemented, these types of electrical systems can provide flexibility and security to a previously vulnerable and rigid infrastructure. A smart grid allows the use of diverse energy resources and can provide solutions to

problems like the charging of electric vehicles. A smart grid brings elements of electricity production, delivery, and consumption closer together (Singer, 2009).

These next-generation electrical grids can automate functions that are traditionally controlled manually which can help with overall efficiency. Smart grids differ from a traditional grid by having a bidirectional flow. The traditional electrical power grid has always flowed electricity from the generation source to the consumers. Smart grids integrate new technology that helps report on the condition and health of the grid. They carry two types of information, one from sensors built into the grid which is delivered to a smart meter and the other is information from the smart meter to the data center of the utility. Information carried from the sensors to the smart meters can be communicated with technology like Wi-Fi or wireless communication standards developed for wireless sensor nodes (WSN). The second type of information can be transferred via Wi-Fi or cellular communication technologies (Tuna et al., 2017).

In this study the current sensor proposed harvests energy from the magnetic field produced by power transmission and distribution lines. This energy harvesting sensor would be utilized to provide power to the wireless sensor nodes it uses to communicate with the smart meter.

1.1.2 Current Sensing Methods

The amount of current flowing through a conductor is a crucial piece of information needed for many electrical applications. There are various forms of measuring current flow and this section will cover the most popular ones. These types of sensors can operate using a variety of sensing techniques which will be covered in this section.

A common and affordable method of sensing current is with a shunt resistor. A shunt resistor utilizes ohms law to measure current flow in a circuit. It senses the voltage drop across the resistor which is directly proportional to the current flow and can be used to measure both AC and DC currents. This type of sensor provides an accurate way of directly measuring AC currents while avoiding complex AC to DC current transformations measurements (Voljc et al., 2009). The shunt resistor must be installed into the current conducting path which can lead to power loss at high currents. Although it is the simplest form of measuring current, a method that provides electrical isolation is typically preferred.

Some of the current sensing methods that are electrically isolated from the conducting path operate by utilizing Faraday's law of induction and by sensing magnetic fields like the Hall-effect sensor does. They both provide a method of sensing current flow without needing to be installed directly into the circuit.

One of the most common sensors that utilizes the principle of induced voltages is called a Rogowski coil. This sensor uses a nonmagnetic core and uses an integrator to get a signal which is proportional to the current that passes through the core (Ripka, 2004). They are also referred to as di/dt coils and are not typically able to measure DC currents. Like many current sensors on the market the core must encircle the conductor to measure the current flow, which can be an inconvenience during installation. In the case of a zip-cord style appliance cord the two wires are placed side by side and are joined by the insulating material. The alternating currents in the two wires are traveling in opposite directions and 180 degrees out of phase so the magnetic field would not be detectable by

a di/dt coil. A Rogowski coil also requires an external power source to operate which can be an issue in reliability.

A current transformer is another sensor that utilizes Faraday's law of induction to measure current. It is very similar to a Rogowski coil but utilizes has a core with a high relative permeability and has a sense resistor integrated into the windings. This allows the current transformer to have an output voltage that is directly proportional to the measured current. There is no integrator required in this type of sensor, so the output signal is compatible with an analog to digital converter (Ziegler et al., 2009). Current transformers cannot measure direct current, so they are typically used in power distribution applications. They also need to fully enclose the current carrying wire and require an external power source. Current transformers are bulky and are made of a large amount of copper and iron.

A hall-effect sensor uses the principle that a current flowing through a conductor which is also subjected to a magnetic flux, produces a voltage perpendicular to the field and to the current. This type of sensor does not operate with an induced voltage generated by a rate of change in current, so it is able to detect magnetic fields that do not change over time. This allows hall-effect sensors to be able to detect direct currents as well as alternating currents. In recent studies a hall-effect sensor capable of measuring high currents has been developed for the rapidly growing market of DC power sources and storages (Faizal et al., 2019). This market is being driven by the increase in electric vehicle usage which use anywhere from 20-40% of current supplied to an average household in the United States. Other advances in this type of sensor have been targeted at making a complementary metal-oxide-semiconductor or CMOS hall-effect sensor for a

low-cost and compact design (Crescentini et al., 2018). These sensors output signal and sensitivity have been improved significantly through methods like designing a combination of switch-type hall elements or a dual-hall sensor scheme (Cheng et al., 2014). Excessive thermal drift is a problem currently encountered in these types of sensors. This can be corrected with multiple calibrations conducted at different temperatures, but this process is labor some and time intensive. Hall-effect sensors also require an external power source to detect currents.

A giant magneto resistive or a GMR sensor senses the presence of a magnetic field by the resistance measured in the active material. This active material is a ferromagnetic and its resistance is determined by the direction and magnitude of an external magnetic field. The GMR current sensors available are core-less which is an advantage over previously mentioned Rogowski coil and current transformer sensors. They show higher sensitivity than hall-effect sensors but are more expensive to implement. Current sensors based on GMR technology have been investigated for the use in smart grids (Ouyang et al., 2019). Compared to the Rogowski coil, current transformer, and hall-effect sensors the GMR sensor seems to be the best suited for this application. GMR sensors require an external power source which is a drawback in some scenarios. They are also likely to be prematurely damaged if an overcurrent situation were to occur.

Other forms of current sensing are based on the Faraday effect observed in light. When a light beam is subjected to a magnetic field oriented parallel to the beam the plane of polarization is rotated. Fiber optic current transformers operate using this principle. Coils of fiber optic cable encircle the current carrying conductor and are not affected by external magnetic fields (Wang et al., 2016). These types of sensors use less power than

conventional current transformers and hall-effect sensor, but still require an external power source. They also have less sensitivity than other sensing methods so are more suited for high amperage applications. The fiber optic cable must be packaged carefully to avoid damage. This is an expensive method of current sensing but has certain applications where the deployment of the sensor would be worth the cost.

1.1.3 Zero-Power Sensor Distinctions

The sensor proposed in this thesis has distinct advantages over previously mentioned devices. The energy harvesting capabilities of the sensor is a feature that other sensors do not have. Because the sensor is passive it does not require an external power source to sense the current on a conductor. In a wireless sensor node with a limited amount of energy the passive nature of the sensor benefits the system. The amount of energy stored by the device determines the number of transmissions per hour a sensor the sensor will be able to send.

Unlike sensors mentioned previously this device does not utilize a yoke that encircles the conductor which is being monitored. Because the method used to sense current is proximity based the sensor does not need to encircle the conductor to detect the magnetic fields produced. Multiple wire configurations can be monitored with this device including two wire appliance cords which typically must be separated for current measurement.

Another advantage over conventional sensors is the overall size. Although some hall-effect and GMR sensors have been made much smaller there are many researchers making these devices on a micro-scale. These types of sensors can be made in batches

which reduces overall cost and material usage. CMOS compatibly opens the door to the use of these sensors on printed circuit boards.

A drawback of utilizing this type of sensor is the piezoelectric ceramic utilized. The sensing element uses lead zirconate titanate (PZT) to harvest energy produced by the conductor. Although it has a high piezoelectric coefficient it can crack overtime. The fatigue life of this material in energy harvesting applications is being studied and shows promise when the material is grown, doped, and processed correctly (Salazar et al., 2020).

The sensor must be placed in an optimal position with respect to the conductor for maximum sensitivity and harvesting capabilities. In this study the spatial positioning will be optimized for the AC current sensor proposed.

1.2 Working Principle

The device proposed in this thesis operates by using a piezoelectric cantilever as a sensing/harvesting element. The cantilever's proof mass magnetically couples with the magnetic field produced by an alternating current flowing through a conductor. This generates an oscillating force on the piezoelectric cantilever which converts mechanical energy to usable electrical energy. This design was first introduced by Richard White and Eli Leland from the University of California, Berkely (Leland, n.d.).

1.2.1 Design Concept

As mentioned previously, the zero-power current sensor proposed in this study operates by using a piezoelectric cantilever to sense the magnetic field produced by a current carrying conductor. The magnetic proof mass placed on the end of the cantilever has two functions. These two functions are to couple with the magnetic field produced by

the current and to tune the natural resonant frequency of the cantilever to 60 Hz which is the frequency of AC current in the United States. The magnetic coupling generates an oscillating force on the piezoelectric cantilever which causes a deflection. This deflection creates stress in the piezoelectric film which converts mechanical energy into AC voltage. The amplitude of this output voltage is directly linked to the deflection of the cantilever. The cantilever is a transducer and provides information on the current that is flowing through the conductor of interest. The schematic below shows the working principle of the device.

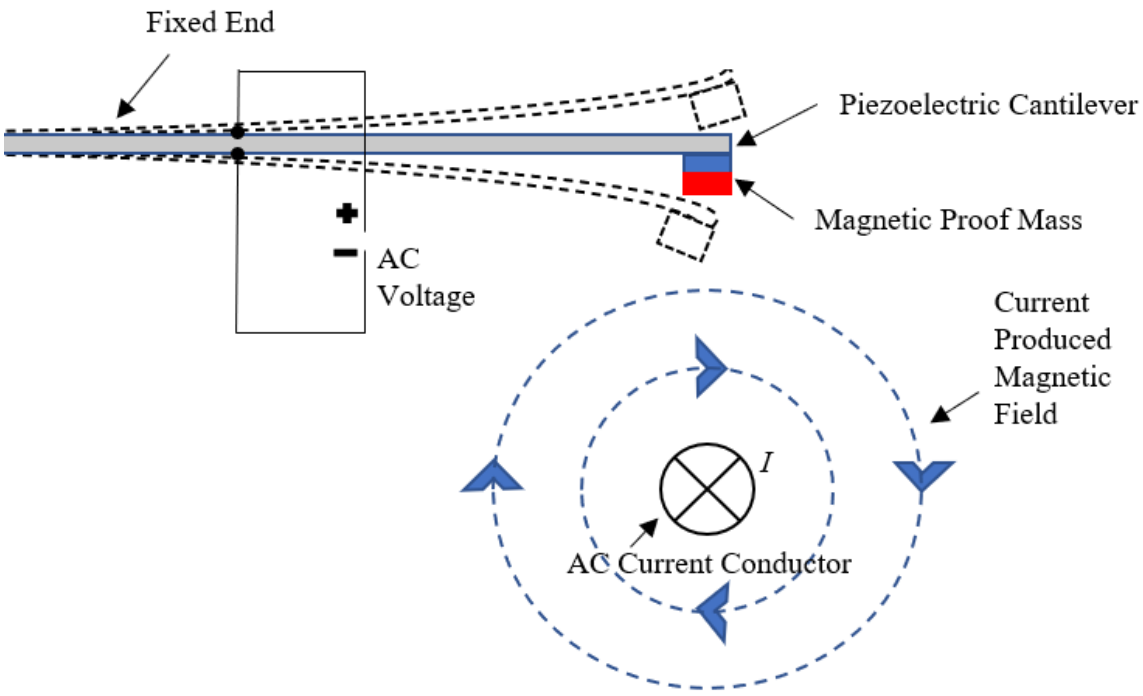

Figure 1. 2: Working Principle of Zero-Power AC Current Sensor

The current sensor will take advantage of the high Q-factor of the cantilever device to provide accurate and high-resolution readings of an alternating current. The high Q-factor also ensures that the device provides high power generation at a certain frequency. The number of oscillations of the cantilever is proportional to the frequency of

the source current. This enables the sensor to detect variations in frequency as well as the magnitude of the current in the conductor.

The magnetic field produced by the current can be described with Ampere's law. In general, Ampere's law states that the closed-path integral of the magnetic flux density $\boldsymbol{B}$, dotted with the differential length of the path, is equal to the permeability of free space μ_o, multiplied by the sum of currents enclosed by said path (Ida & Bastos, 1997). This is shown with the Equation (1).

$$\oint \boldsymbol{B} \cdot d\boldsymbol{l} = \mu_o \sum I_{in} \qquad (1)$$

For a long straight wire, we can assume the magnetic field produced is circular around the conductor, following the right-hand rule. If the path integrated is in the same direction and along the magnetic field produced, the dot product is equal to 1 and the magnetic field is uniform. Equation (1) is simplified to Equation (2) shown below which states that a conductor produces a magnetic field whose strength is inversely proportional to the radial distance from the nearest point on the conductor.

$$\oint \boldsymbol{B} \cdot d\boldsymbol{l} = \mu_o \sum I_{in} = \boldsymbol{B} 2\pi r = \mu_o I_{in}$$

$$\boldsymbol{B} = \frac{\mu_o I_{in}}{2\pi r} \qquad (2)$$

The current carrying conductor is parallel with the z-axis in the coordinate system used. As mentioned before, the wire is long and straight so we can assume the magnetic field varies radially but is uniform along the z-axis. The magnitude of the position vector $\boldsymbol{r} = x\boldsymbol{i} + y\boldsymbol{j}$ inserted into Equation (2) can be used to describe the magnetic field produced. Equation (3) describes the magnetic field produced at a radial distance from the conductor. Fig. (1.3) depicts a schematic of the coordinate system used for the

derivation, the radial position vector with respect to the conductor, and the components of the magnetic field vector.

$$B = \frac{\mu_o I_{in}}{2\pi\sqrt{x^2+y^2}} \qquad (3)$$

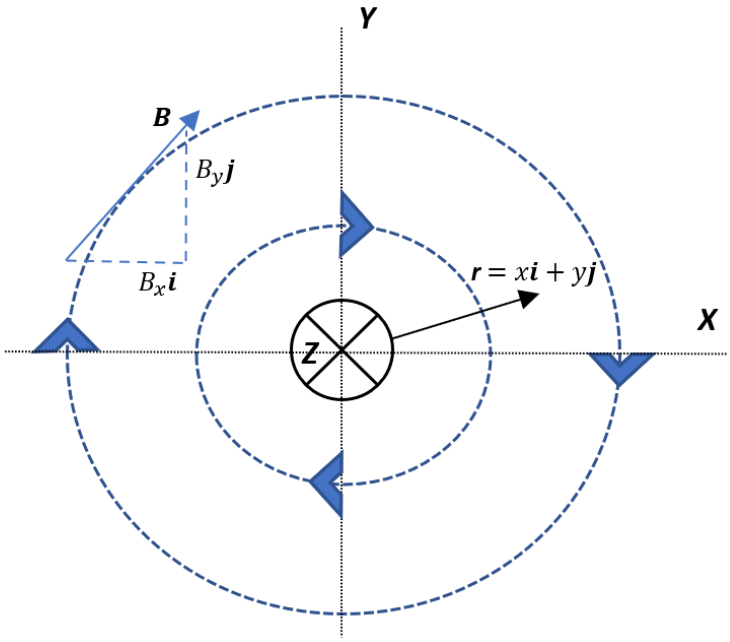

Figure 1. 3: Position Vector and Magnetic Field Vector Components

The magnetic field described by Equation (3) produces a force on the magnetic proof mass attached to the tip of the cantilever. This force $\boldsymbol{F}$ can be described with the Equation (4) which is for the force on a magnetic dipole in an external magnetic field (Knoepfel, 2008), where $\boldsymbol{m}$ is the dipole moment and $\boldsymbol{B}$ is the external magnetic field.

$$d\boldsymbol{F} = \nabla(\boldsymbol{m} \cdot \boldsymbol{B})dV \qquad (4)$$

Taking the integral over the volume of the magnet *V*, with a remanence $\boldsymbol{M}$ Equation (4) yields the following which gives the total force:

$$\boldsymbol{F} = \int \nabla(\boldsymbol{M} \cdot \boldsymbol{B})dV \qquad (5)$$

The total force produced by the magnetic field can be separated into components and since the field does not vary along the conductor, we can omit the force generated in that direction.

$$\boldsymbol{F}_x = \int \left[\boldsymbol{M} \cdot \frac{\delta \boldsymbol{B}}{\delta x}\right] \boldsymbol{i}\, dV$$

$$\boldsymbol{F}_y = \int \left[\boldsymbol{M} \cdot \frac{\delta \boldsymbol{B}}{\delta y}\right] \boldsymbol{j}\, dV$$

$$\boldsymbol{F}_z = \int \left[\boldsymbol{M} \cdot \frac{\delta \boldsymbol{B}}{\delta z}\right] \boldsymbol{k}\, dV = 0$$

The magnetization of the magnet in this study has been oriented such that it is aligned with the y-axis that is demonstrated in Fig. (3). This reduces Equation (5) to the following:

$$\boldsymbol{F} = \boldsymbol{F}_x + \boldsymbol{F}_y = \int \left(\left[\boldsymbol{M}_y \cdot \frac{\delta \boldsymbol{B}_y}{\delta x}\right] \boldsymbol{i} + \left[\boldsymbol{M}_y \cdot \frac{\delta \boldsymbol{B}_y}{\delta y}\right] \boldsymbol{j}\right) dV \quad (6)$$

Both the horizontal and vertical forces exerted on the magnetic proof mass are considered with Equation (6). The forces are proportional to the gradient of the magnetic field in the y-direction. The y-component of the force generated by the external magnetic field is greatest approximately where the magnetization vector of the magnet and the radial position vector make a 45° angle. The x-component of the force is greatest where the magnetization vector and the radial position vector are parallel and perpendicular. Fig. (1.4) below depicts the positions where the magnitudes of the gradient of the magnetic field with respect to the x and y-axis are greatest. The magnitude decreases radially and is constant along the z-axis.

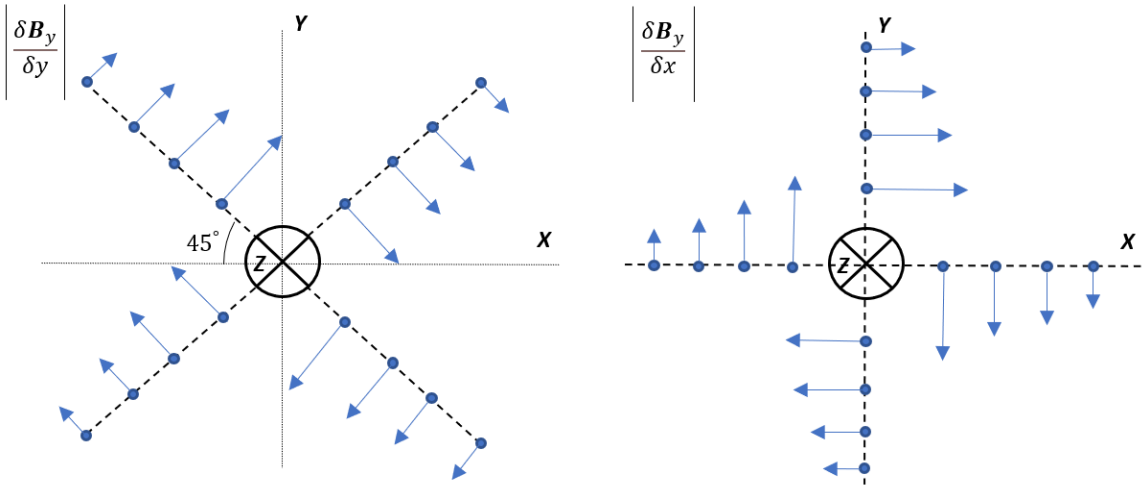

Figure 1. 4: (left) Magnitude of y-Component Gradient of the Magnetic Field (right) Magnitude of x-Component Gradient of the Magnetic Field

The theory that all forces exerted by the magnetic field generate a net torque on the cantilever have been studied and compared to works that only considered the vertical force exerted on the magnetic proof mass (Houlihan et al., 2019) (Houlihan et al., 2016). The lateral and vertical forces that act on the permanent magnet described in Equation (6) are two of the three forces that generate the net torque. The third force exerted on the magnet by the external magnetic field is caused by magnets tendency to rotate into the magnetic field. This magnetic torque acts about the center of the magnet and makes a substantial contribution to the net torque. A magnet with a remanence $\boldsymbol{M}$, in an external magnetic field $\boldsymbol{B}$, generates a magnetic torque τ_m and is described by Equation (7).

$$\tau_m = \int \boldsymbol{M} \times \boldsymbol{B}\, dV \qquad (7)$$

With the assumption that the magnetization of the proof mass is along the y-direction it can be further simplified to Equation (8) which shows that the magnetic torque is proportional to the lateral component of the current produced magnetic field $\boldsymbol{B}_x$.

The lateral component of the magnetic field is maximized directly above and below the current carrying conductor.

$$\tau_m = \int \boldsymbol{M}_y \cdot \boldsymbol{B}_x \, dV \quad (8)$$

Together these three forces generate the net torque at the fixed end of the cantilever and are the described in Equation (9). The lateral magnetic force $\boldsymbol{F}_x$, generates a force that is dependent on the thickness of the magnetic proof mass t_m and the vertical force $\boldsymbol{F}_y$, generates a force dependent on the location of the magnet. This relationship is described by Equation (10).

$$\tau = \tau_{F_x} + \tau_{F_y} + \tau_m \quad (9)$$

$$\tau = \int_l^{l+l_m} F_y dx + \int_{-t_m}^{0} F_x dy + \tau_m \quad (10)$$

Fig. (1.5) is a schematic which depicts how the net torque is generated on the cantilever. The magnetic proof mass is placed at the same location for all trials of the experiment. The magnet thickness will be varied which will cause a significant change in net torque. All forces that cause a torque act over the volume of the magnetic proof mass so as the thickness increases so will the forces.

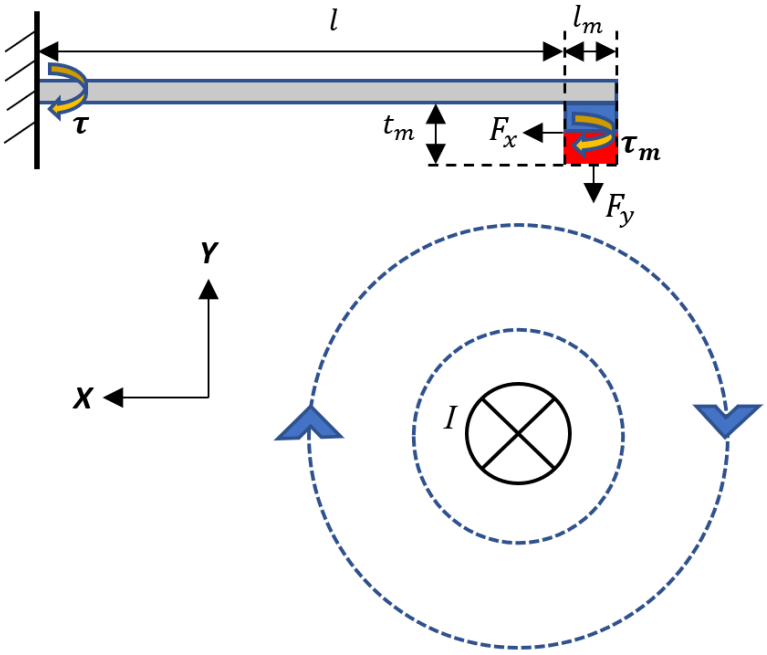

Figure 1. 5: Torque Generated by the Forces Acting on the Permanent Magnet

1.2.2 Applications

The zero-power current sensor proposed in this study can be utilized in smart grids, commercial, or industrial applications. Real-time monitoring of conditions in the electric grid improves security and reliability. Sensors are needed to monitor important parameters like temperature, current, and frequency. These sensors need power to transmit data via a WSN. Most smart grids rely on sensors that are powered by batteries, but the sensor proposed in this study is self-sufficient which means it will produce its own power. It can detect small variations in high ampere power transmission lines as well as changes in frequency. The device proposed could also be utilized as an energy harvester to power other necessary sensors.

1.3 Previous Works

Recently, researchers have proposed magnetic-piezoelectric coupled energy harvesters and sensors with various designs. The design concept was first proposed by

Richard White and Eli Leland from the University of California, Berkely (Leland, n.d.). The concept works well for sensing both AC and DC currents (Wang et al., 2017) (Wang et al., 2017) as well as powering wireless sensor nodes. The concept has been proven to be effective on the macro and micro scale. In this thesis design parameters are optimized on a macro-scale to provide insight when designing microelectronic mechanical system (MEMS) devices.

1.3.1 Energy Harvesters

The need to power wireless devices that are typically powered by batteries has created a large research effort to find alternative power methods. Many alternatives have been proposed like solar powered devices which perform very well in some instances but lack in others (Roundy et al., 2003). Studies have shown that a piezoelectric cantilever can be utilized to harvest energy from mechanical vibrations that would otherwise be wasted (Roundy & Wright, 2004). The application of these vibrational energy harvesters would be in HVAC ducts, manufacturing equipment, or household appliances. The demand for smaller and CMOS compatible harvesters lead to the design and fabrication of MEMS energy harvesters. Numerous MEMS kinetic energy harvesters have been investigated over the past decade to power wireless sensor networks (Andosca et al., 2012) (Jackson et al., 2014) (Choi et al., 2006). Whether at the macro or micro scale, the high Q-factor associated with a cantilever is a disadvantage in applications where the driving frequency varies by a substantial amount.

A high Q-factor is an advantage when harvesting energy from alternating current in the electric grid because it deviates a small amount. This method is applicable for scavenging energy from electric power systems and is an attractive alternative to coil-

based methods (Paprotny et al., 2013). Unlike coil-based scavenging methods, magnetic-piezoelectric coupled energy harvesters can be used to harvest energy from household appliance cords (Leland et al., 2006). The zip-cord style conductors have two wires that are physically bound with the insulation. The alternating current flowing through each wire have magnetic fields that are equal in magnitude and opposite in directions which make it difficult for a coil-based scavenger to detect a magnetic field. The proximity-based sensing style of the magnetic-piezoelectric coupled energy harvesters is ideal for this situation and many others where the conductor consist of more than one wire. MEMS energy harvesters have also been developed for this application and are CMOS compatible which makes manufacturing of the harvester more efficient and affordable (Olszewski et al., 2017).

The device proposed in this study can act as a power source for a wireless sensor node and as a current sensor. Previous studies have used similar piezoelectric cantilevers to power temperature sensor and to transmit the data collected wirelessly (Yeh et al., 2021) (Wang et al., 2021). A resonant frequency of 60 Hz was achieved by tuning the cantilever. This method yielded an optimal power output by producing maximum deflection of the cantilever. In this study the desired resonant frequency was attained by adjusting the mass of the magnetic proof mass but other methods of tuning, like spring supported cantilevers, have surfaced and show promise by providing fine adjustment to the resonant frequency (Wang et al., 2022).

1.3.2 AC Current Sensors

When the magnetic-piezoelectric energy harvester is placed near a current carrying conductor the deflection experience by the cantilever is proportional to that

current. The voltage produced by the piezoelectric cantilever is the output of the transducer. The alternating magnetic field created by AC current produces a sinusoidal force on the cantilever which then oscillates at the same frequency. Therefore, the sensor proposed in this study can detect both changes in the frequency and amplitude of the source current. Recent studies have reported on the use of this technology to monitor AC and DC currents while supplying power to a WSN (Wang et al., 2017) (Wang et al., 2017). The sensor developed in this study is for AC current only but could be adapted to measure direct current.

This type of sensor has many advantages over the conventional non-contact current sensors which are mentioned in previous sections, but one of the most notable is the fact that it can be self-sustained. The devices that utilize this method of sensing occupy less space. The concept has been proven to have acceptable resolution while being much smaller (>100x) than conventional current sensors (Lao et al., 2014). Even smaller MEMS AC current sensors were designed and fabricated to measure single-wire and two-wire zip-cords. These MEMS sensors exhibited linearity and enough power to run the signal conditioning circuit (Leland et al., 2009) (Leland et al., 2010) (Olszewski et al., 2014).

The placement of the magnetic proof mass relative to the current carrying conductor is critical to obtaining optimal sensor performance. The location of the cantilever is related to the force which is directly dependent on stress/strain of the piezoelectric material. Optimal placement has been investigated in previous studies and is dependent on factors such as the placement of the magnet along the cantilever, the dimensions of the magnet, and the mechanical properties of the cantilever (Houlihan et

al., 2016) (Houlihan et al., 2019) (Aragonez & Jackson, 2021). Other researchers have proposed a correction scheme for positioning and orientation errors (Xian et al., 2017) (Xian & Wang, 2017). Although the correction scheme does reduce the error in measurements, it utilizes an array of cantilevers which calls for more material and larger overall dimensions of the device. The error in single cantilever can be mitigated by careful orientation and calibration of the sensor.

1.4 Focus of Study

The focus of this study is to develop a prototype zero-power AC current sensor. The sensor can be utilized to detect current and frequency changes in an alternating current or used to power a wireless sensor network for the transmission of data. This concept has been investigated by others as demonstrated in the previous section. It has proven to be a viable way to sense current and harvest energy from the magnetic fields produced by current carrying conductors.

In this study certain design parameters not considered in previous works will be investigated and optimized. The mechanical properties of the piezoelectric cantilever are analyzed experimentally by comparing output voltages and resolutions of different devices. The number of piezoelectric layers in the device and the spring constants of the cantilevers are a few of the mechanical properties considered while designing the sensor. The optimal spatial positioning of the permanent magnet and cantilever in relation to the conductor is investigated. Optimal positioning is found by maximizing the magnetic flux through finite element modelling as well as experimentally by measuring peak voltage output from the piezoelectric cantilever.

Power lines used in smart grids come in various sizes and configurations. This study investigates the effects of varying the configuration from single bare wire to a stranded wire. The type of conductor is rarely considered so this study collected and analyzed data for different configurations and gauges.

1.4.1 Vision and Objectives

The zero-power sensor developed in this study is able to detect changes in the mA range for the current being measured. The sensor can detect changes in current frequency of less than 0.1 Hz. The resolution observed with this device varies with the mechanical properties of the piezoelectric cantilever utilized as the transducer. The selection of a cantilever with mechanical properties that maximize resolution and power output will optimize the sensor for the desired application.

The sensor has many advantages over other current sensor in that it is passive with no external energy source required. It is proximity based which means it is electrically isolated from the circuit being monitored. This reduces the amount of power loss and allows the sensor to measure conductors with more than one wire.

This thesis documents the optimization of design parameters for a zero-power current sensor and the effects conductor type has on its performance. Energy scavenging and current sensing is explored through computational simulations and experimentally. It includes the simulation of the magnetic interaction between the proof mass and different conductor types; experimental validation of the simulation; manufacturing of the prototype sensor; and the characterization of the sensor.

Chapter 2: Simulation

A computational model of every experimental scenario was created using the software COMSOL Multiphysics. To visualize the magnetic field produced by a stranded and solid conductor, they are the analyzed in the software. Conductors of various diameters are compared to one another.

The magnetic proof mass is then added to the model to analyze the coupling between the mass and the magnetic field produced by the current carrying conductor. The software is used to predict the optimal spatial location of the magnetic mass with respect to the conductor.

2.1 Configuration of Computational Models

Each computational model utilized in this study is setup and configured to simulate the interaction between the magnet field produced by the current and that of the hard magnet used to tune the resonant frequency of the cantilever. The size of the magnetic proof mass is held constant for all simulations. The thickness of the magnet was selected by considering the average thickness used in the experimental portion of this study. Another driving factor in the selection of the magnet thickness was the need to simulate forces experienced in magnets with higher aspect ratios.

Using the assumption that the current carrying conductor is long and straight, a two-dimensional analysis is sufficient to capture an accurate representation of the magnetic field produced. The computational power required to run this type of analysis is reduced and the time of each simulation is lesser than that of a 3-dimmensional model.

This simplification is possible because the Lorentz forces that produce the deflection in the cantilever are constant in the direction perpendicular to the current in the wire.

2.1.1 Physics Module

A stationary study is done for this model which means it is not dependent on time. The ‘AC/DC’ module in COMSOL Multiphysics is utilized to construct this finite element model. This module is used to compute electric and magnetic fields in static and low-frequency systems. There are many different physics packages that can be imported to the model but for this system the best is the electromagnetic fields package.

The default model inputs are all set at standard temperature and pressure. The temperature of the air, copper, and N42 magnet is 293.15 K. The pressure is 1 atm in the model. Although the temperature of the conductor increases with current in the experimental scenario, the copper temperature is raised to 1000 K in the simulation with no difference in the magnetic flux density produced.

2.1.2 Governing Equations

The physics module solves Maxwell’s equations which are formulated using magnetic vector potential. The equations shown below are the differential form of Maxwells equations (Knoepfel, 2008). Maxwell’s first and second equations are a form of Gauss’s law. Equation (11) states that the electric flux through a closed surface is proportional to the charge enclosed. Equation (12) states that the net magnetic flux through a closed surface is equal to zero, due to the principle of flux traveling from one pole to the other. Equation (13) is Faraday’s law which states a changing magnetic field will produce an electromotive force in wire. Equation (14) is the Ampere-Maxwell law

which is Ampere's law with a term called displacement current added. This extra term takes changing electric flux into account.

$$\nabla \cdot \boldsymbol{D} = \rho_e \qquad (11)$$

$$\nabla \cdot \boldsymbol{B} = 0 \qquad (12)$$

$$\nabla \times \boldsymbol{E} = -\frac{\delta \boldsymbol{B}}{\delta t} \qquad (13)$$

$$\nabla \times \boldsymbol{H} = J + \frac{\delta \boldsymbol{D}}{\delta t} \qquad (14)$$

2.1.3 Geometry

Due to the 2-dimmensioal simplification, the magnet is modeled as a square, the solid conductor is a circle, the stranded conductor is a cluster of 7 circles coincident with one another, and a larger circle representing the air encircles all geometries. The larger circle has a diameter of 1 meter. The material of the conductor is assigned as copper and material properties like conductivity, relative permeability, and relative permittivity are auto assigned from the software's data base.

2.1.4 Boundary Conditions

The 'Magnetic Fields' physics package is used to model electrically induced magnetic fields in coils, conductors, and magnets. To solve the variables that describe the direction of the current, a 'Coil-Geometry Analysis' must be selected and properly setup within the model. For this study the wire is assigned to be a single conductor coil with 0 turns. For the solid conductor, the coil selection is the circular domain which represents the cross-sectional view of the conductor. An example of how this domain should be selected is shown in Fig. (2.1). In the stranded model the seven circular domains that represent the individual strands of the conductor must all be selected as the coil. Once the

wire is assigned as a coil, a coil current can be set to the 60A targeted in the experimental setup. The circles that represent the conductor cross section are assigned the material of copper so that the properties like conductivity are registered by the Coil-Geometry Analysis'.

Fig. (2.1) below depicts the appropriate domain selection of the 'Magnetic Fields' physics package and the coil selection. The air surrounding the conductor and magnetic proof mass is modeled by a 1-meter diameter circle and should be included in the domain selection. The conductor has a fixed position is constrained at the center of the circle. The proof mass is the component of the model that is swept horizontally.

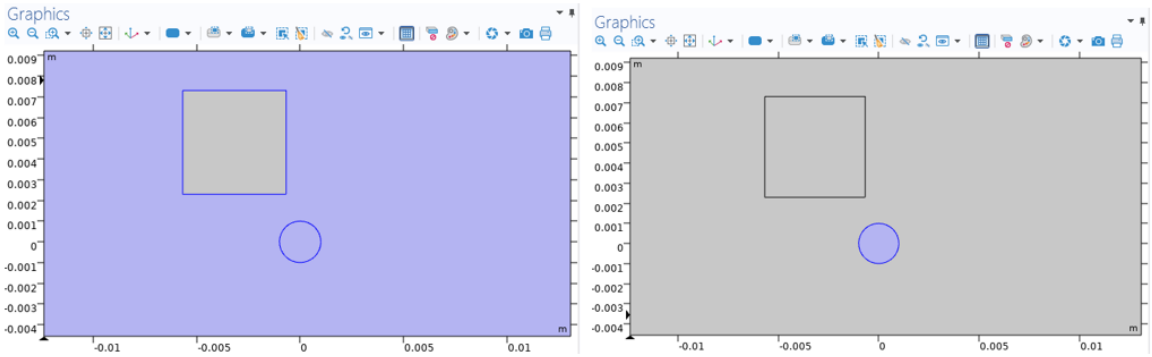

Figure 2. 1: (left) 'Magnetic Fields' Domain Selection. (right) 'Coil' Domain Selection

The magnetic field produced by the magnetic proof mass is not induced by the current, so the magnet itself should not be included in the 'Magnetic Fields' physics module domain selection. The magnets material should be assigned as N42, and incorporated into a separate 'Magnetic Fields, No Current' physics module. The domain selection of this module is depicted in Fig. (7). To define the magnet, the module required another domain to be added. This was done from the physics tab and is called 'Magnetic Flux Conservation 2' and the magnet was added to the selection. Fig. (2.2) shows the domain selection which includes only the magnet.

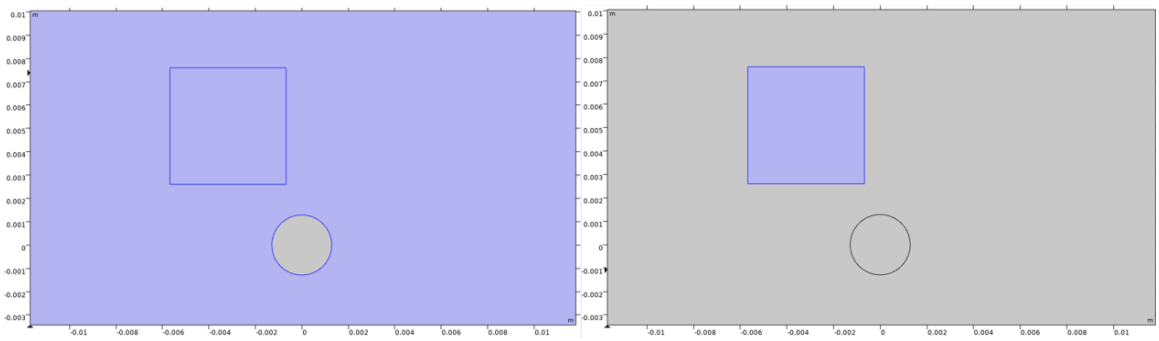

Figure 2. 2: (left) 'Magnetic Fields, No Current' Domain Selection. (right) 'Magnetic Flux Conservation 2' Domain Selection

The last modification was changing magnetization model within this new domain to ‘Remanent flux density’ since material properties of N42 contains ‘Recoil Permeability’ and ‘Remanent Flux Density’. This module has 'Magnetic Flux Conservation 1' but only the air domain was included here, and the magnetization model remained ‘Relative Permeability’. Fig. (2.3) shows a screen capture of the model builder and where to change the magnetization model settings.

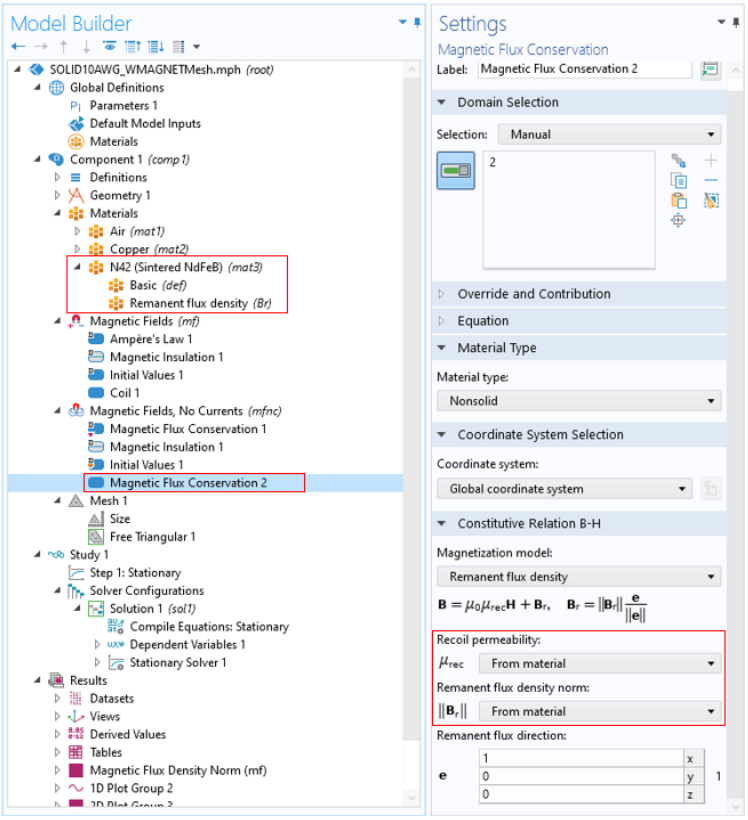

Figure 2. 3: Magnetization Model Settings for 'Magnetic Flux Conservation 2'

2.2Mesh Configuration

The meshing of all structures was done before the simulation was executed. The type of mesh utilized was a free triangular mesh which denotes the shape of each individual mesh element. The 2-dimmensional analysis produces a less computationally expensive model which allows for a finer mesh to be used. All models in this study used an extremely fine mesh setting to produce more accurate results.

2.2.2 Mesh Configurations for Conductor

The mesh produced for the model of a solid conductor with no magnetic mass has 33,190 domain elements and has 348 edge elements. The mesh size parameters are equivalent for all simulations done and are shown in Table (1.1) below. Fig. (2.4) shows

the final mesh that was generated for this model. Due to the simplicity of this scenario the model was able to produce accurate results with a larger mesh element size.

Table 2. 1: Mesh Size Parameters for Solid 10 AWG Conductor

Max. Element size	.02 m
Min. Element size	.00004 m
Max. Element Growth Rate	1.1
Curvature Factor	0.2
Resolution of Narrow Regions	1

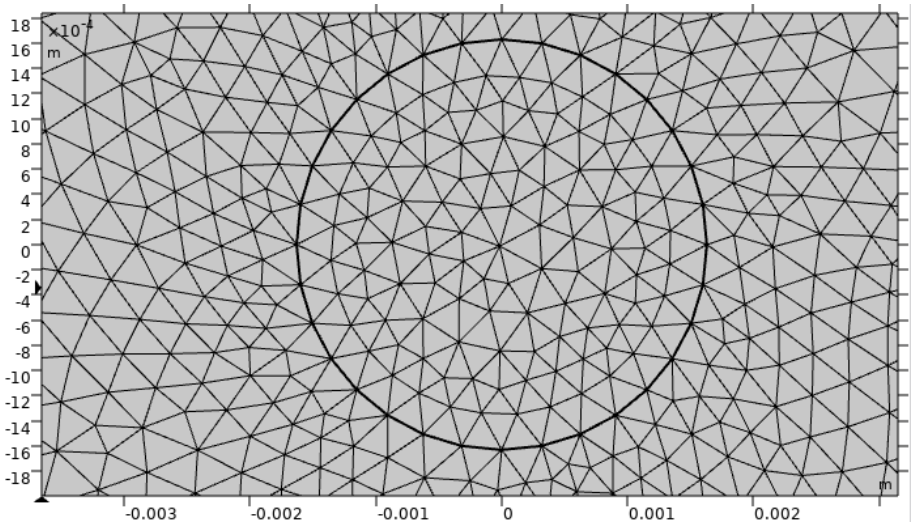

Figure 2. 4: Mesh Generated for Solid 10 AWG Conductor

The mesh for produced for the model of a stranded conductor with no magnetic mass has 51,456 domain elements and has 933 edge elements. The mesh size parameters are shown in Table (2.2) below. Fig. (2.5) shows the final mesh of the model which has smaller elements than that of the solid conductor due to the complexity of the scenario.

Table 2. 2: Mesh Size Parameters for Stranded 10 AWG Conductor

Max. Element size	.0134 m
Min. Element size	.00006 m
Max. Element Growth Rate	1.3
Curvature Factor	0.3
Resolution of Narrow Regions	1

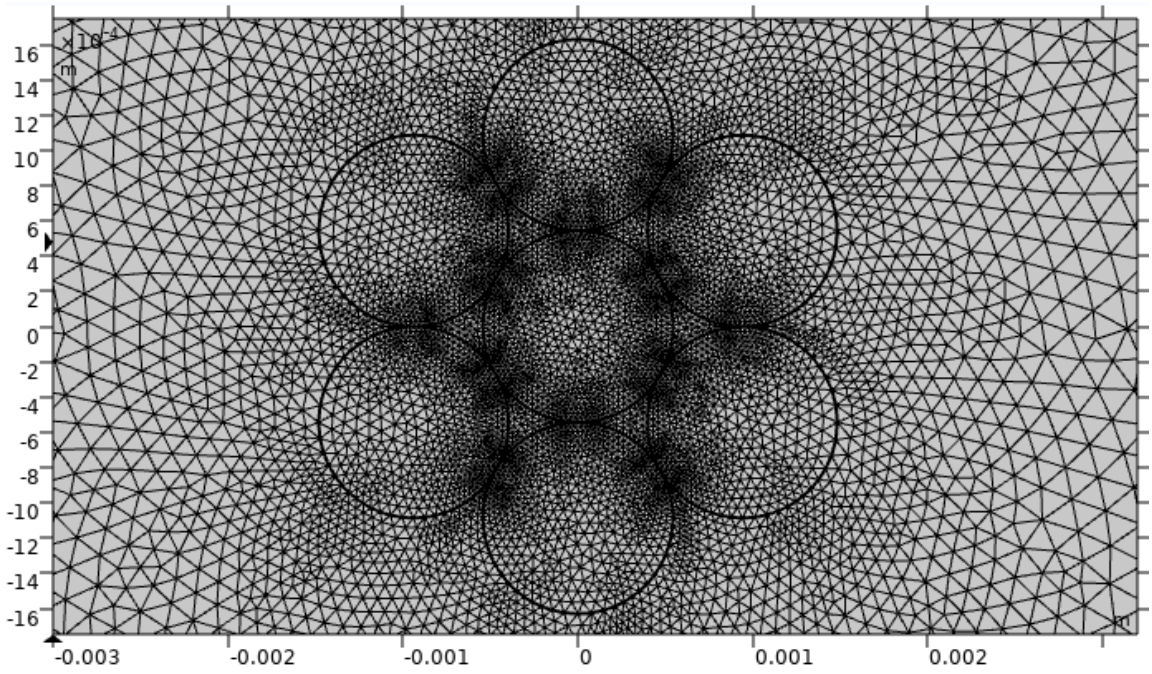

Figure 2. 5: Mesh Generated for Stranded 10 AWG Conductor

2.2.2 Mesh Configuration for Conductor and Magnet

The mesh produced for the model with a solid conductor and the magnetic proof mass consisted of 35,628 domain elements. This mesh had a total of 403 edge elements. The other mesh size parameters are the same as those in the model for the conductor alone and are shown in Table (2.1). Fig. (2.6) below shows the final mesh produced for the solid conductor and magnet.

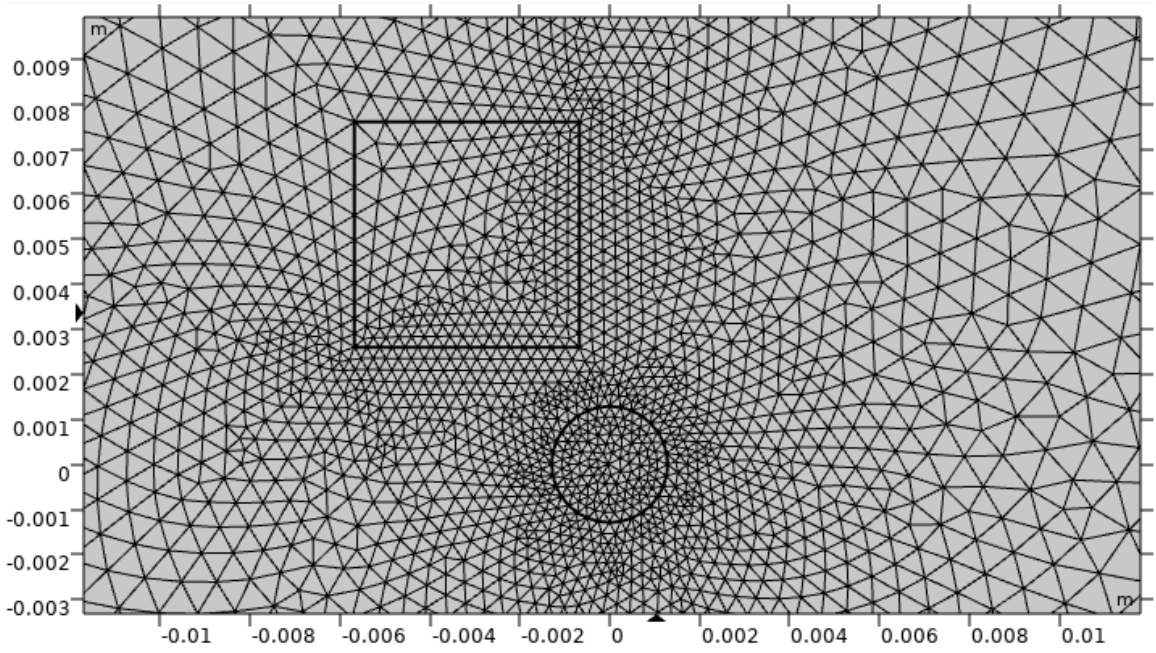

Figure 2. 6: Mesh Generated for Solid 10 AWG Conductor and Magnet

The mesh produced for the model with a stranded conductor and the magnetic proof mass consisted of 73,744 domain elements. This mesh had a total of 1511 edge elements. The other mesh size parameters are the same as described in the Table (2.2) above. The mesh for this model has more domain elements where the strands of the conductor coincide. This mesh was produced by the physics module which is what the software recommends for the model. Fig. (2.7) below shows the complete final mesh and below that Fig. (2.8) is a closer view of the stranded conductor within the same model.

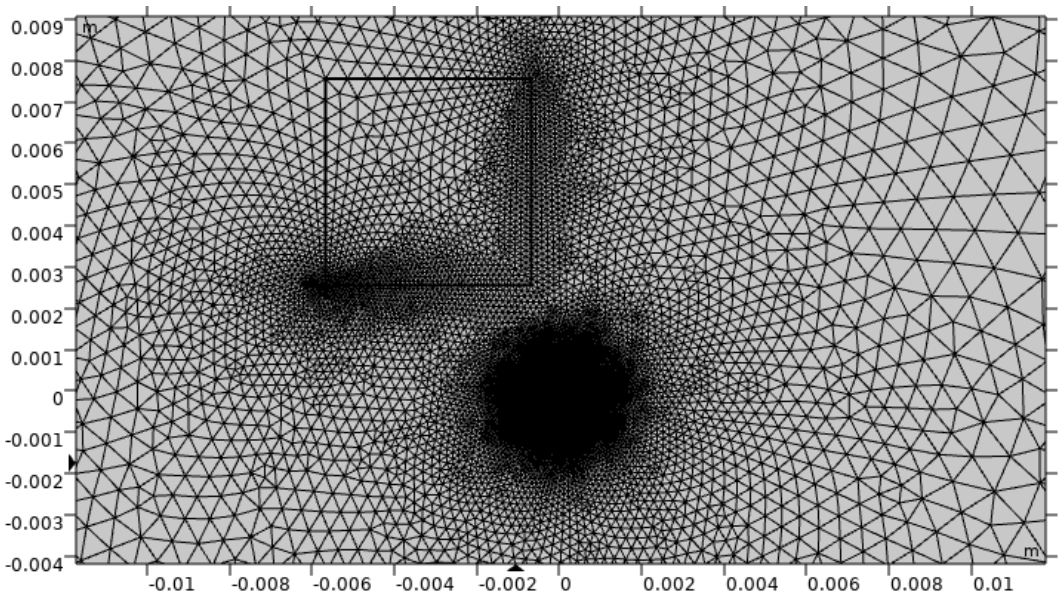

Figure 2. 7: Mesh Generated for Stranded 10 AWG Conductor and Magnet

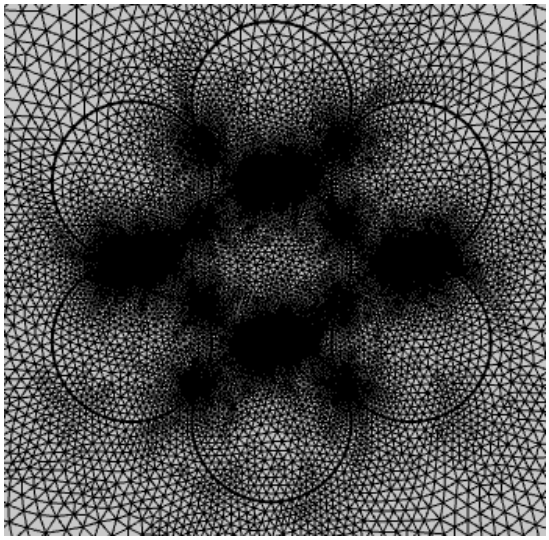

Figure 2. 8: Closer View of Mesh Generated for Stranded 10 AWG Conductor and Magnet Model

2.2.3 Results of Conductor Simulation

The magnetic fields produced by the stranded and solid conductors are compared with an arrow surface study. This study uses arrows to create a visualization of the direction and magnitude of magnetic flux density calculated. The arrows are proportional in size to the amount of flux observed at that point. Fig. (2.9) shows an example of the

arrow surface studies done on the 10 AWG wires. The magnetic flux density observed in the solid conductor is greater than that calculated in the stranded model. The maximum value in the solid conductor model is 10.3 mT, while the maximum value for the stranded configuration is 10.1 mT.

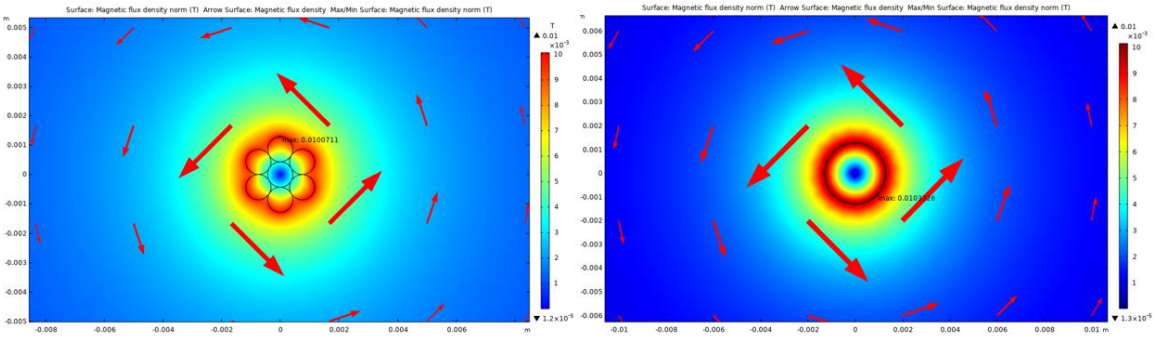

Figure 2. 9: Arrow Surface Study for (left) Solid 10 AWG Wire (right) and Stranded 10 AWG Wire

The trend of the solid conductor showing higher magnetic flux densities is observed for all gauges of wire utilized in this study. The magnetic flux density produced by each conductor is inversely proportional to the diameter. The 10 AWG conductors have the smallest diameter considered in this study and produce the highest magnetic flux density. The results of the study are tabulated and shown in Table (2.3) below.

Table 2. 3: Magnetic Flux Density as a function of Wire Gauge

	Solid Conductor (mT)	Stranded Conductor (mT)
10 AWG	10.3	10.1
8 AWG	8.07	7.95
6 AWG	6.41	6.27

2.2.4 Results of Conductor and Magnet Simulation

Once the models of the conductor alone were made and verified, the integration of the N42 magnet was made possible. The optimal position for the magnet with respect to the center of the conductor was found by varying the x position or the distance from the

center of the conductor. The parameter of interest in the model is magnetic flux density and is measured in tesla. The maximum value of magnetic flux density indicates the position in which coupling between the current produced magnetic field and that of the magnet is optimal for cantilever deflection.

The dimensions of the magnetic proof mass were constant for all conductor types and gauges. The magnet was modeled as a square with a side length of 5 mm to better simulate forces experienced with high aspect ratio magnets. Lorentz forces in the x direction and magnetic torque produced by the magnet are more prominent in magnets that have this geometry. It was placed at a height or y coordinate of 1.27 mm from the uppermost point of the conductor. The reason this coordinate was not taken with respect to the center of the conductor is because of the different gauges of conductors utilized in this study. Using the distance from the center of the conductor, while keeping the height constant, would place the magnet closer to the conductor for larger gauges.

The x position of the magnetic proof mass was varied using a parametric sweep. The magnet's center of mass is positioned at various x positions in increments of 0.635 mm or 0.025". Although the resolution limits of the software are very small, the sweep is conducted using similar increment values used to verify the results experimentally. The resolution of translation stages used to position the cantilevers was used to determine the minimum resolution of the parametric sweep in the simulation. Using a reasonably attainable resolution on the x axis allowed for the proper comparison of the simulation results and those obtained in the experimental portion of this study.

The optimal placement of the magnetic proof mass varied with conductor diameter but not with conductor configuration. Although the optimal positioning of the

magnet remained consistent for stranded and solid conductors the values of magnetic flux density did vary. The solid conductor produced higher values than that produced by the stranded for all cases. For the 10 AWG conductors the solid conductor produced a magnetic flux density of 20.96 mT and the stranded conductor produced 15.55 mT with the magnetic proof mass placed at x = 3.175 mm from the center of the conductor. This shows a decrease of 25.8% in magnetic flux density from a solid to a stranded conductor which is proportional to the force that would act on the cantilever. Fig. (2.10) and Fig. (2.11) depict the optimal placement of the solid conductor and stranded conductors.

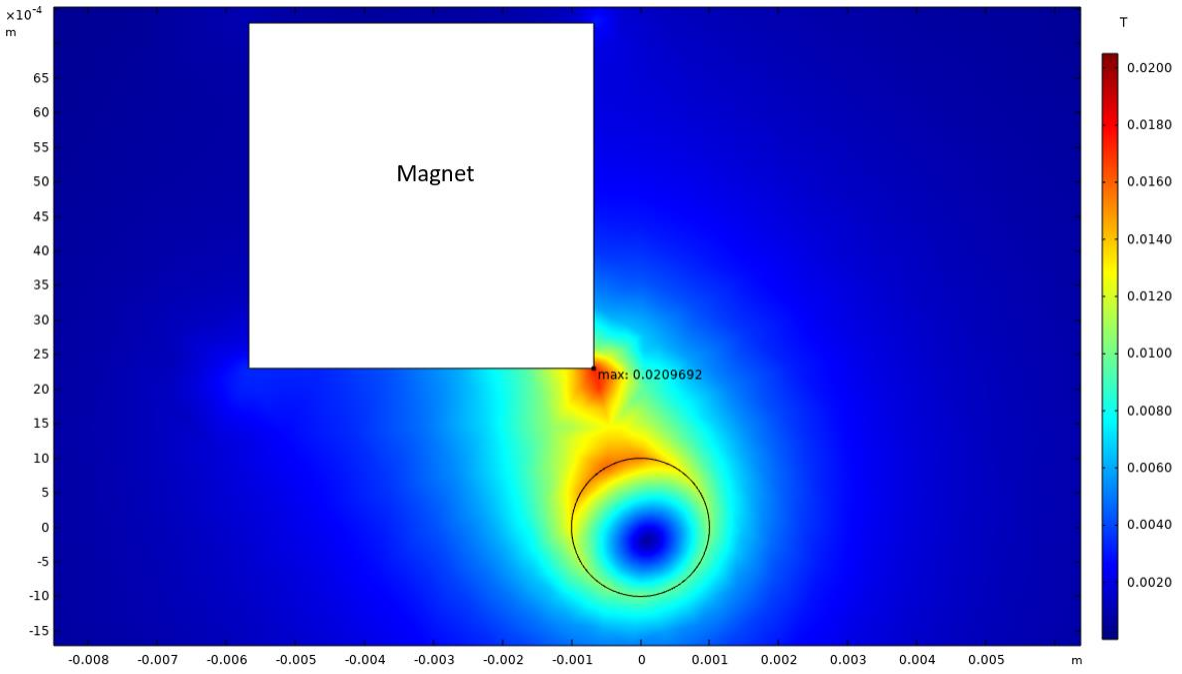

Figure 2. 10: Optimal Magnetic Mass Placement for 10 AWG Solid Conductor

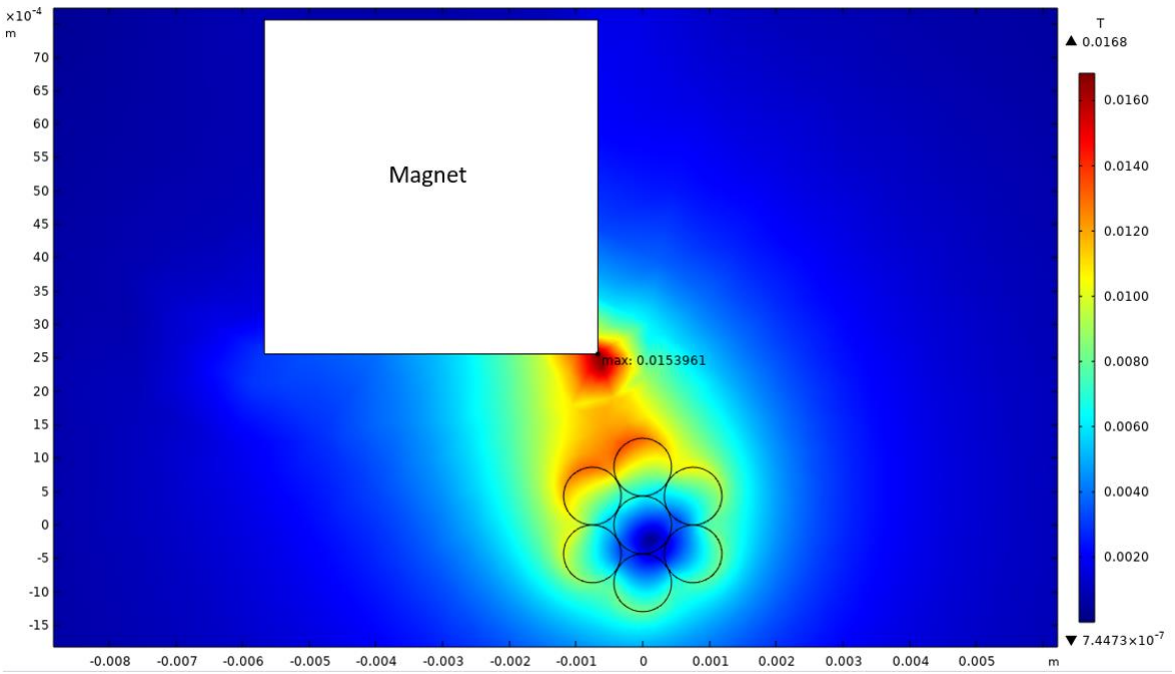

Figure 2. 11:Optimal Magnetic Mass Placement for 10 AWG Stranded Conductor

Further computational studies conducted showed that the topological differences between the two wire configurations contributes to the magnitude of the Lorentz forces that act on the proof mass. The stranded conductor is made of seven individual strands which produce a different magnetic field than the solid conductor does. Each strand of the stranded conductor produces a hemispherical magnetic field. The size of the field produced is reliant on the diameter of each strand and the amount of current flowing through the conductor. The topological effect produced on the overall magnetic field is reduced as the diameter of the individual strands decreases and as the current increases.

An arrow surface study uses arrows to indicate the direction and magnitude of magnetic flux density at different points in the model. This arrow surface study was conducted on both solid and stranded conductors to analyze the resultant magnetic field produced with the magnetic proof mass. The dimensions and the positioning of the

magnetic proof mass were constant in all computations. Thus, the fluctuations in the magnetic flux density were a result of the wire type only. This allowed the proper analysis of the coupling between the magnet and the current produced magnetic field.

The model for the stranded 10 AWG conductor at 60A, reveals that the strands are large enough to cause an interaction between the individual strands in the presence of the magnetic field of the proof mass. This interaction between individual strands can be observed in Fig. (2.12) below.

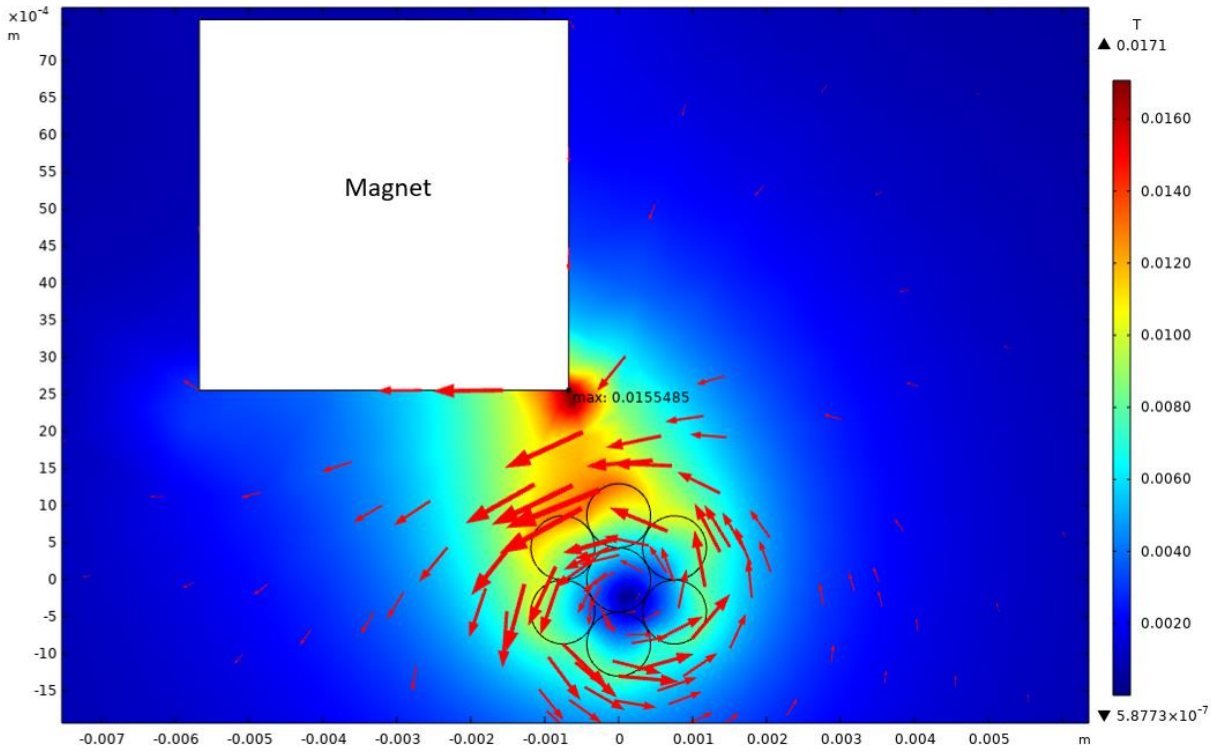

Figure 2. 12: Arrow Surface Study for Stranded 10 AWG Wire and Magnet

The computational model for the solid conductor indicates a larger magnetic flux density near the magnet. Since the arrow size is proportional to the magnitude of the magnetic flux in that area, the larger arrows show areas where maximum magnetic coupling is occurring. The largest areas of magnetic coupling for the solid conductor occur near the magnetic proof mass while the areas near the conductor are smaller and

more uniform in size and can be observed in Fig. (2.13). The direction of the flux near the magnet had more of a y component than the flux arrows shown in the stranded model. The largest arrow shown in the solid conductor simulation makes a 42° angle with the magnet while the largest arrow in the stranded model near the magnet makes a 33° angle.

Other forces that cause a torque on the cantilever are caused by the x gradient of the magnetic field and magnetic torque produced by the remanence of the proof mass. The magnetic torque acts through the center of the proof mass and is counterclockwise in the current position of the magnet. The magnetic torque causes the cantilever to deflect upwards in this configuration. The forces produced by the x gradient of the magnetic field are maximized while the proof mass is centered directly above the conductor. This means that although they are present, the most influential forces are the magnetic torque force generated by the magnet and the force in the y direction caused by the magnetic field of the wire (Houlihan et al., 2019).

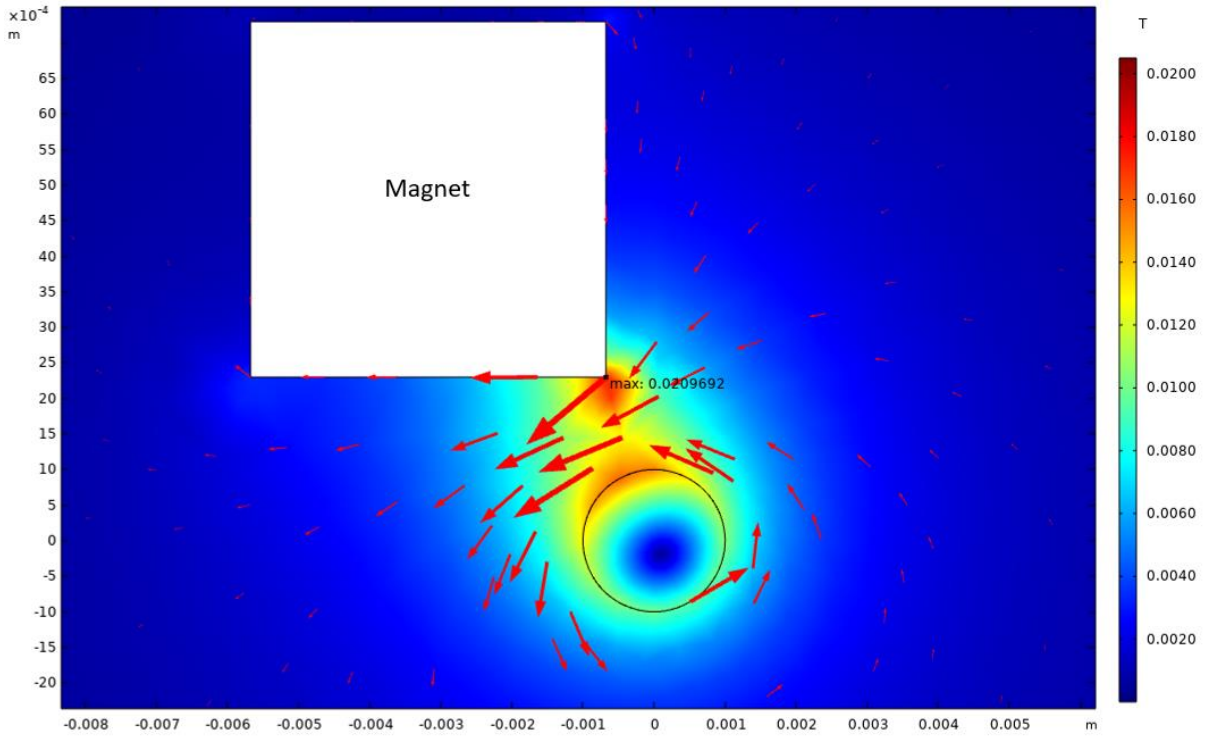

Figure 2. 13: Arrow Surface Study for Solid 10 AWG Wire and Magnet

The optimal placement of the magnetic proof mass is dependent on the gauge of the conductor being used to provide the source current. Both solid and stranded conductors of the same gauge had the same optimal placement in the simulations conducted. The larger diameter conductors produced lower magnetic flux densities than those of the smaller. This means the magnetic coupling for larger conductors is lower and less force is applied to the cantilever. The smaller deflections would mean less power produced and less resolution for the sensor. Optimal positioning of the magnetic proof mass for solid conductors is shown in Fig. (2.14). Fig. (2.15) shows the same but for stranded conductors of varying gauges.

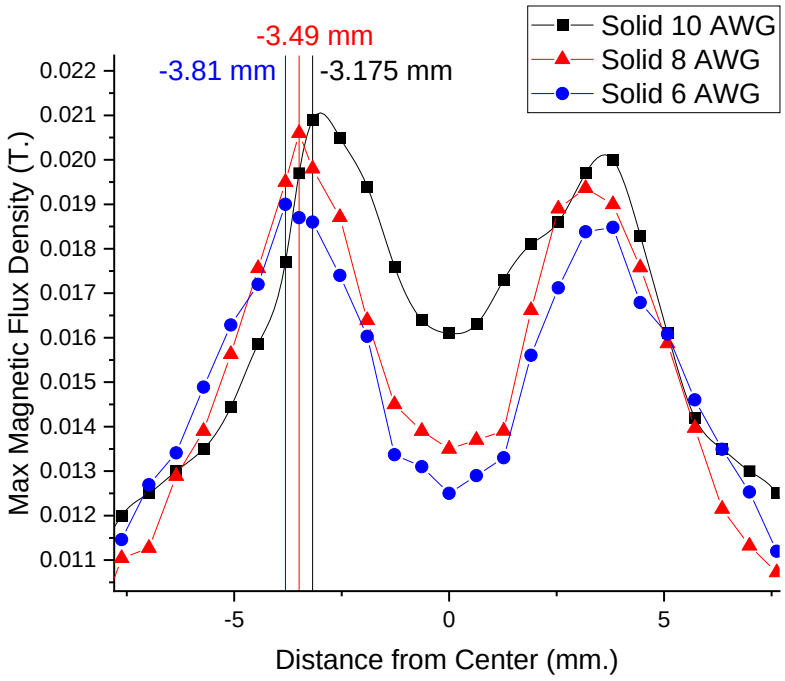

Figure 2. 14: FEM Optimal Positioning of the Magnetic Proof Mass for Solid Conductors

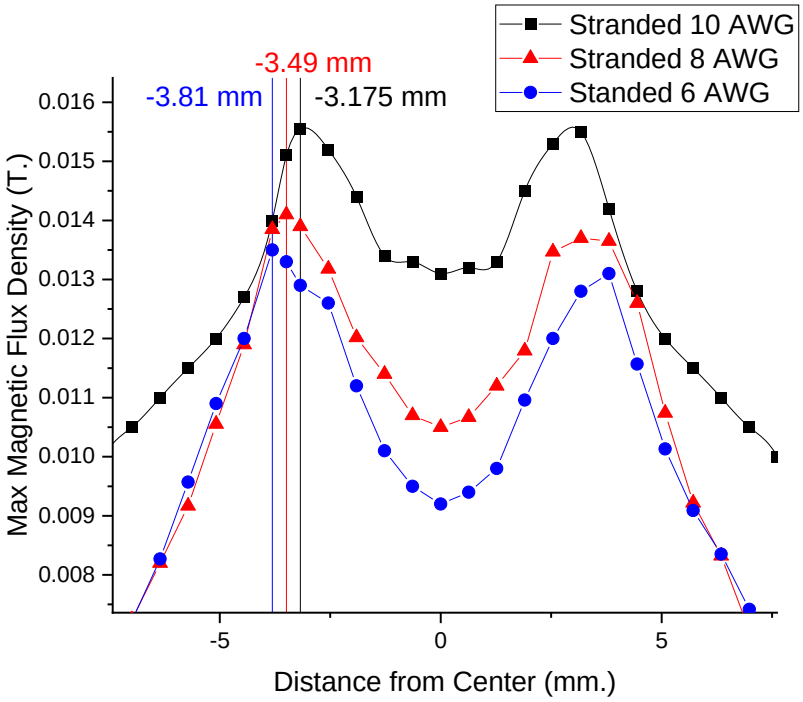

Figure 2. 15: FEM Optimal Positioning of the Magnetic Proof Mass for Stranded Conductors

The results of the simulation show the optimal angle of the magnet with respect to the conductor. The angle is defined with the magnetization vector of the magnet and the radial vector with the center of the conductor. The magnetization vector is placed at the center of the conductor and points in the positive y direction as shown in Fig. (2.16) below.

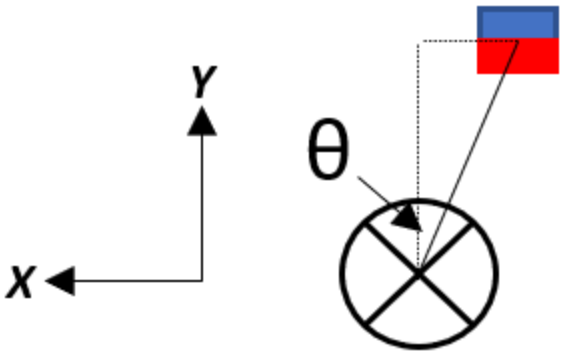

Figure 2. 16: Schematic of Optimal Magnet Angle

The stranded and solid 10 AWG conductor had the optimal placement of x = -3.175 mm from the center of the conductor. This placement of the magnet makes for a 40.1° angle with the conductor. The 8 AWG conductors had the optimal placement of x = -3.49 mm while the 6 AWG conductors showed optimal placement of x = -3.81 mm. The spatial coordinates of the magnet in the simulations produce angles of $\theta = 42.3^{\circ}$ for the 8 AWG conductors and $\theta = 45.3^{\circ}$ for the 6 AWG conductor.

Previous investigations modeled the force on a permanent magnet by a current carrying wire (Leland et al., 2010). The model was developed with the principle that the force on a magnet in a magnetic field is proportional to the gradient of that magnetic field. The magnetization of the magnet is assumed to be in the y direction and the remanence is assigned to create a force density field. The author states that only the y directed force field is considered for their analysis, which produces a maximum force at $\theta = 45^{\circ}$. For

this simulation, all forces produced by the interaction between the magnet and the current produced magnetic field are considered.

Chapter 3: Experimental Setup

3.1 Spatial Positioning Scheme

To have a reproduceable experiment, the current carrying wire must be in the same position for every trial. Regarding spatial positioning of the magnetic proof mass, the only parameters that can vary are the height and distance to the conductor. The center of the conductor is used as the origin of the coordinate system utilized for this experiment. For simplicity the coordinate system is reduced to a plane or a 2-dimmensional system. The magnetic field produced by the current carrying conductor is the same in the direction parallel to the current flow. The spatial coordinate, z, which pertains to this axis is omitted from the study. The height of the magnetic proof mass is translated along the y axis and the distance from the center of the conductor is along the x axis. The schematic below shows the coordinate axis utilized to position the magnetic proof mass.

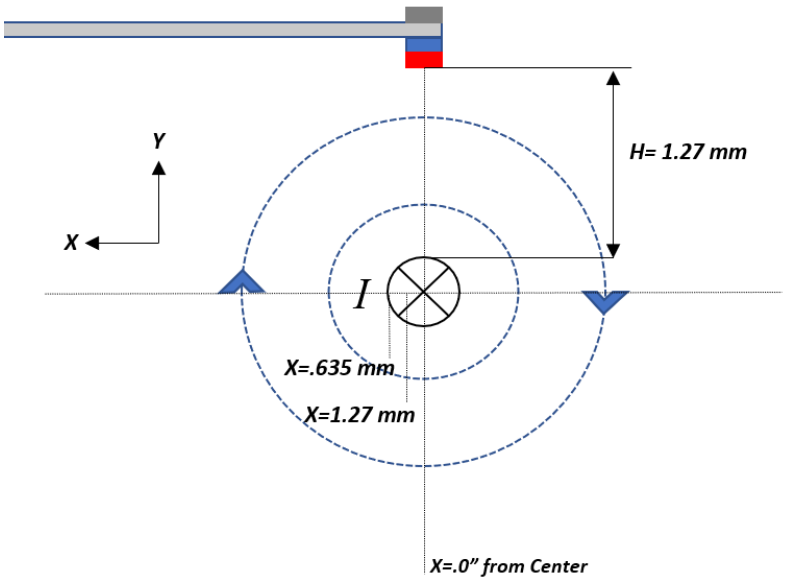

Figure 3. 1: Schematic of Coordinate System Utilized

3.1.1 Translation Stages

A custom-made experimental setup was developed to position the cantilever near the current carrying wire. The spatial positioning of the magnetic proof mass was varied with a micromanipulator translation stage (Thorlabs DTS50). Two stages were mounted orthogonally to one another using a bracket also manufactured by Thorlabs. The stages provide a maximum resolution of 0.635 mm (.025”) in the x and y-directions. The distance from the bottom of the mass to the wire was kept constants for all experiments in this study. The height of the magnet was 1.27 mm (.050”) to allow for deflection under maximum source current without a collision occurring between the wire and the magnetic mass. The translation stage assembly was them mounted at a plate of aluminum (9”x7”x.25”). This plate ensures that the assembly maintains its position and the orthogonal angle of approach with the conductor.

3.1.2 Experimental Fixtures

A fixture was designed to hold the cantilever to the translation stages. The fixture had the design requirements of both clamping the cantilever firmly to produce a repeatable effective length and to mitigate flexion. If flexion of the fixture occurred, it would rob the sensor of power and compromise the optimal placement of the magnetic proof mass. The fixture was designed in Solidworks and manufactured with a 3D printer. The material chosen for this fixture was ABS plastic for its durability and resistance to flexion. Fig. (3.2) below shows the fixture and translation stage assembly in Solidworks as well as the final product.

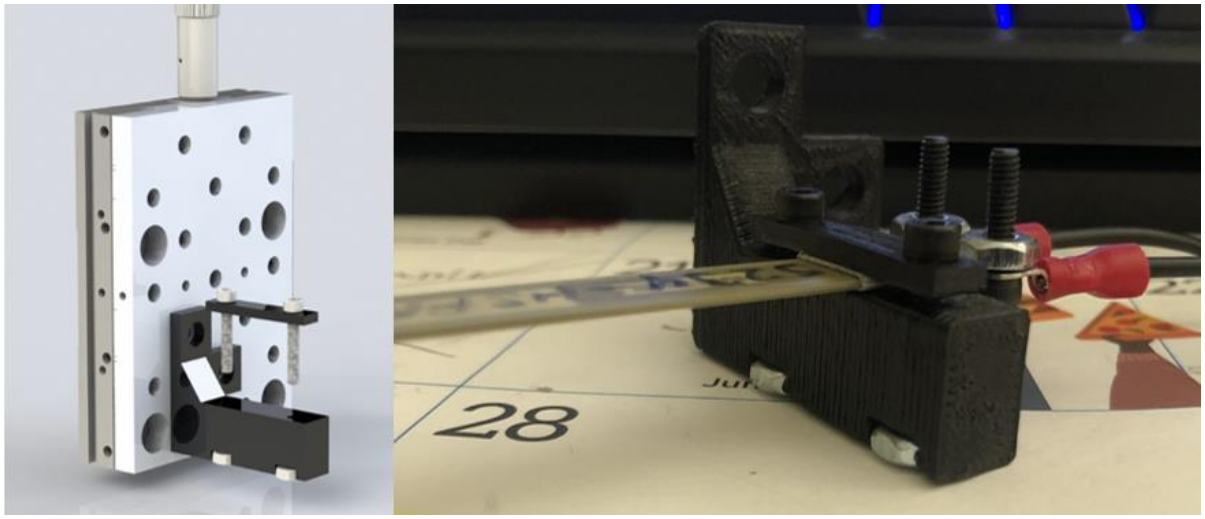

Figure 3. 2: (left) CAD Model of Fixture (right) Fixture and Hardware Utilized to Mount Cantilevers

The wire is suspended in the air at a fixed location with two 3D printed clamps that ensure it is in the same place for every experiment. The conductor must not contact the aluminum plate that the translation stage assembly was mounted to. This would cause a short circuit and could be very dangerous for the researcher. All metal surfaces, including the mounting plate are insulated with a rubber film to prevent arching. The clamps can secure wires that range from 4 to 20 AWG. The material selected for these wire clamping fixtures is ABS plastic. The temperature of the wire being held should not exceed 100 ℃. This was confirmed using the smallest gauge wire acquired for this study with the maximum amount of current the custom-made setup could produce.

Using the two translation stages and the fixtures previously described, the cantilever is swept horizontally along the x axis in increments of 0.635 mm. This sweep is performed to determine the effects on varying the spatial location of the magnetic proof mass with respect to output voltage of the device.

3.2 Electrical Setup

The source current in this experimental setup is modeled after the current flowing through the conductors used in a smart grid. The target frequency is 60 Hz but varies in some experiments to gauge the sensitivity of the proposed sensor. The goal of the custom electrical setup was to obtain as much as 60A of current, but the system was only able to produce 30A. Although the current in most of the grid is alternating current, for the validation and testing of this sensor a pulsed direct current was used. The response of the device to both types of current was analyzed, and the results indicated that the pulsed direct current setup produced similar values to that of the alternating current setup. Fig. (3.3) below shows the entire setup utilized for this sensor characterization.

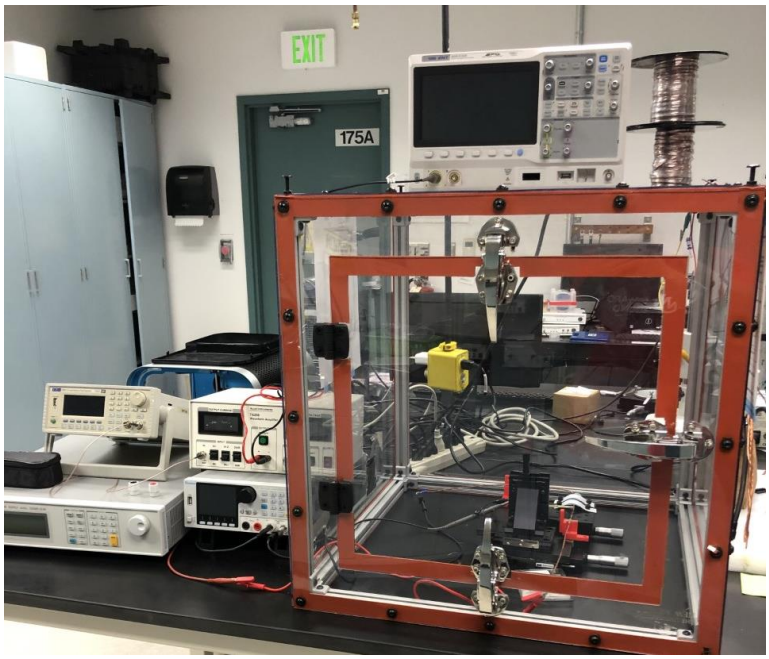

Figure 3. 3: Custom-Made Setup with a Safety Enclosure

3.2.1 Alternating Current Setup

A function generator was used to validate the DC pulsed current setup. The function generator (Aim-tti Instruments TG5011) can produce a variety of waveforms

like sine, square, ramp and more. To simulate the alternating current, a sine waveform was utilized. The maximum output level of this device 10 mV_{pp}-10 V_{pp} into 50 Ω, which is a maximum of 0.4A. This level of amperage is far too small to be able to test our device so the function generator was paired with a waveform amplifier (Accel Instruments TS250) to produce a 5A sinusoidal wave. Fig. (3.4) shows how the devices mentioned previously are connected to one another for the AC setup.

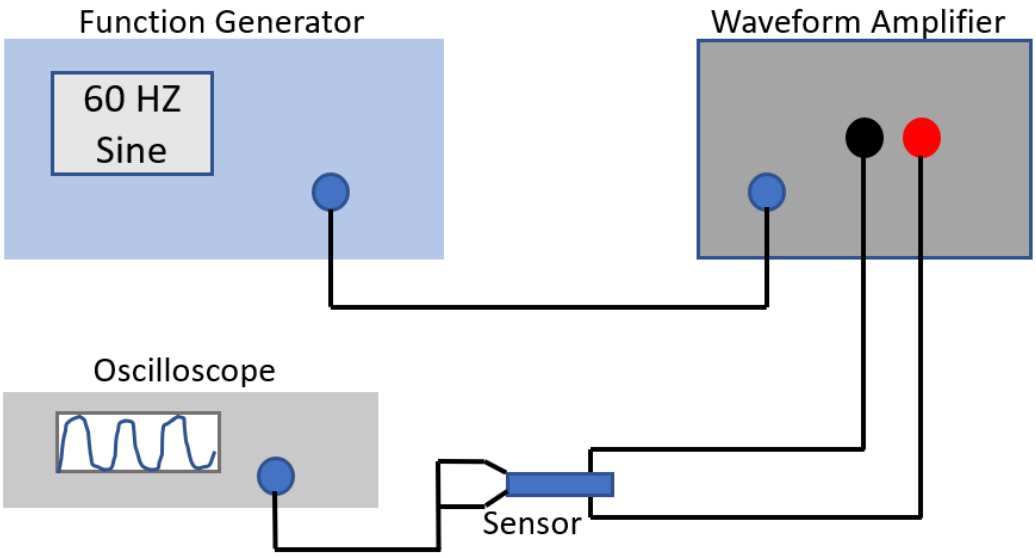

Figure 3. 4: AC Setup Schematic

This AC waveform was used as a source current for the sensor. The AC frequency creates a magnetic field that is changing direction and magnitude with time. The open-source voltage produced by the sensor was measured with an oscilloscope. The sine wave produced by the function generator and waveform amplifier was also measured with an oscilloscope and is shown in Fig (3.5).

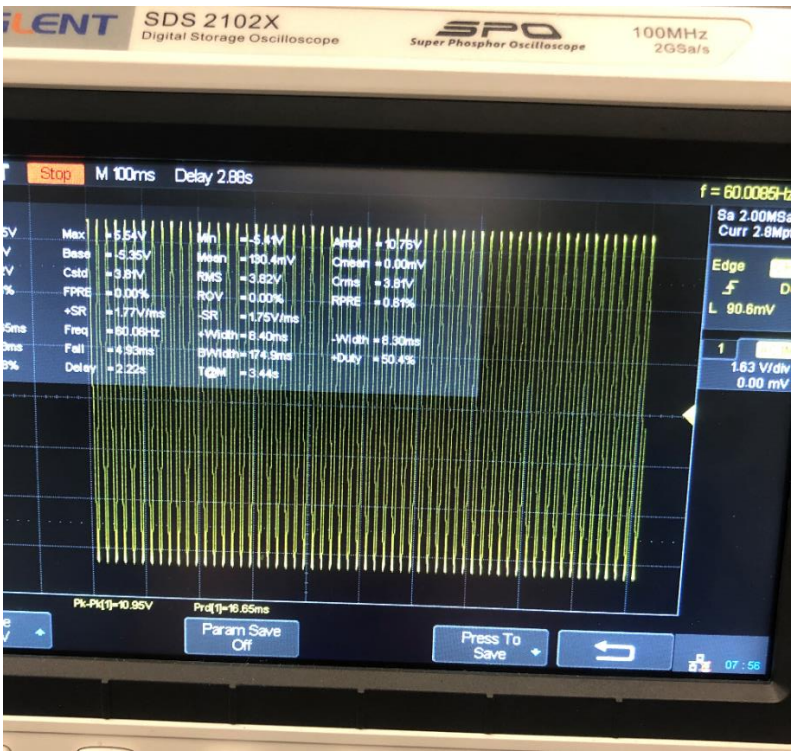

Figure 3. 5: Waveform Produced by AC Setup

A clamp-style ammeter was used to validate the source current in this setup. The readings taken by the ammeter were very close to 5 A and varied only slightly. The AC current setup is shown in action by Fig. (3.6) below.

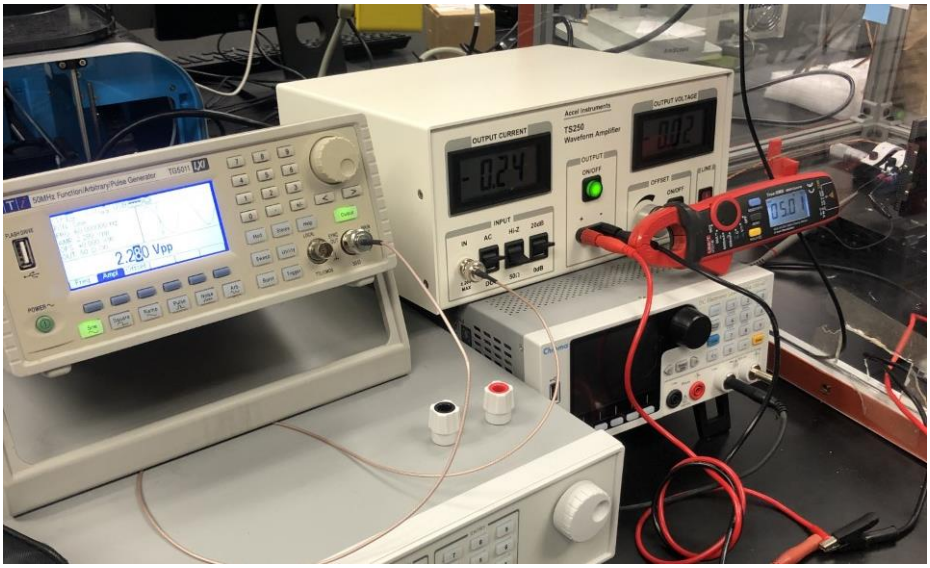

Figure 3. 6: Ammeter Utilized to Verify Current in AC Setup

3.2.2 Pulsed DC Setup

A DC power supply (Chroma 62006P-30-80) is utilized to supply the source current to the conductor in this setup. This unit can deliver 80A of current and is modulated with an electronic load (Chroma 63004-150-60). The electronic load was used to create a pulsed DC waveform. By altering the period of the signal, the frequency was set to 60 Hz to simulate the magnetic field that what would be produced by a conductor in a smart grid.

The electronic load must be operated in 'Constant Current Dynamic' or CCD mode which allows the user to set parameters for the amplitude and duration of each pulse. One of the parameters used to adjust the frequency was the pulse width of the signal on the electronic load. This model of electronic load utilizes two pulse width settings indicated by the variables 'TI' and 'T2'. The sum of the two pulse width settings is equal to the period of the waveform produced. The CCD mode used in this experimental setup can control pulse width up to .001 ms which provides a maximum resolution of .0072 Hz. For the experiments conducted in this study a pulse width increments were .01 ms for a resolution of .075 Hz. Adjusting this parameter was necessary to determine the sensor's sensitivity to changes in source current frequency.

The other parameter adjusted on the electronic load was the level of current commanded by the unit. In CCD mode, there are two levels of current that can be controlled. They are labeled 'L1' and 'L2' and are the levels of current seen for pulse widths 'T1' and 'T2' respectively.

To acquire a waveform with the target frequency of 60 Hz a pulse width of 8.333 ms is set for both 'T1' and 'T2' and the current is set to 0A for 'L1' and the desired

amplitude of the source current for ‘L2’. Fig. (3.7) depicts the settings used for the target frequency.

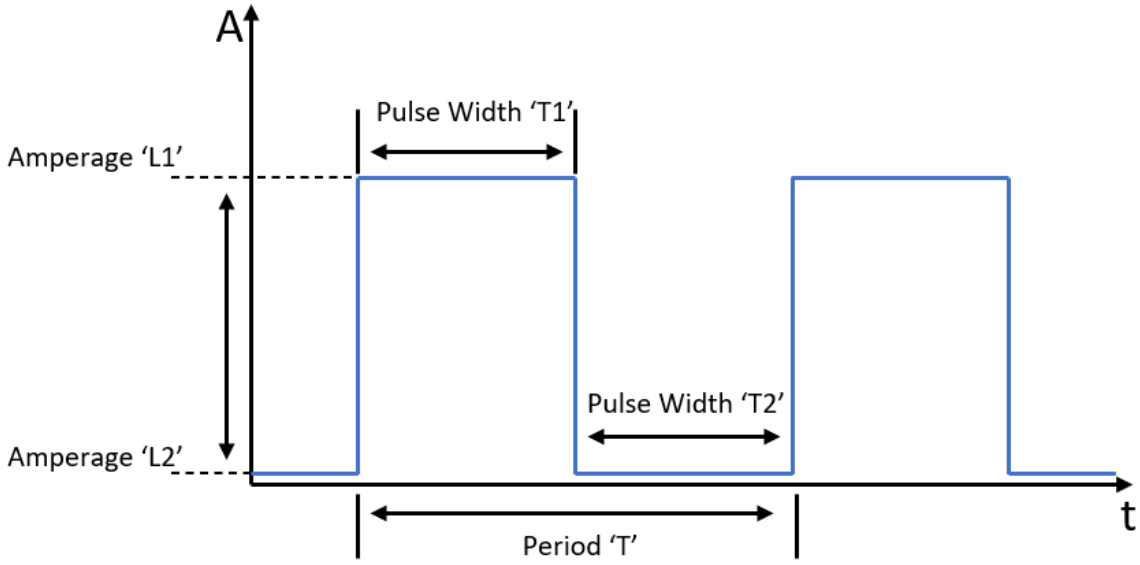

Figure 3. 7: Schematic for DC Pulsed Setup Parameters

The pulse width was set to 10 ms in Fig. (3.8) below for demonstration purposes. The oscilloscope was used to analyze the waveform and ensure the rise and fall times of the electronic load were set accordingly. If the rise and fall times of the unit were too slow then the waveform would resemble a “sawtooth” wave and the frequency of the waveform would be compromised.

Figure 3. 8: Waveform Produced by DC Setup

The clamp-style ammeter also had the ability to measure frequency and was used to verify the accuracy of the pulsed DC configuration. The schematic below depicts how the components of the system are wired to function properly.

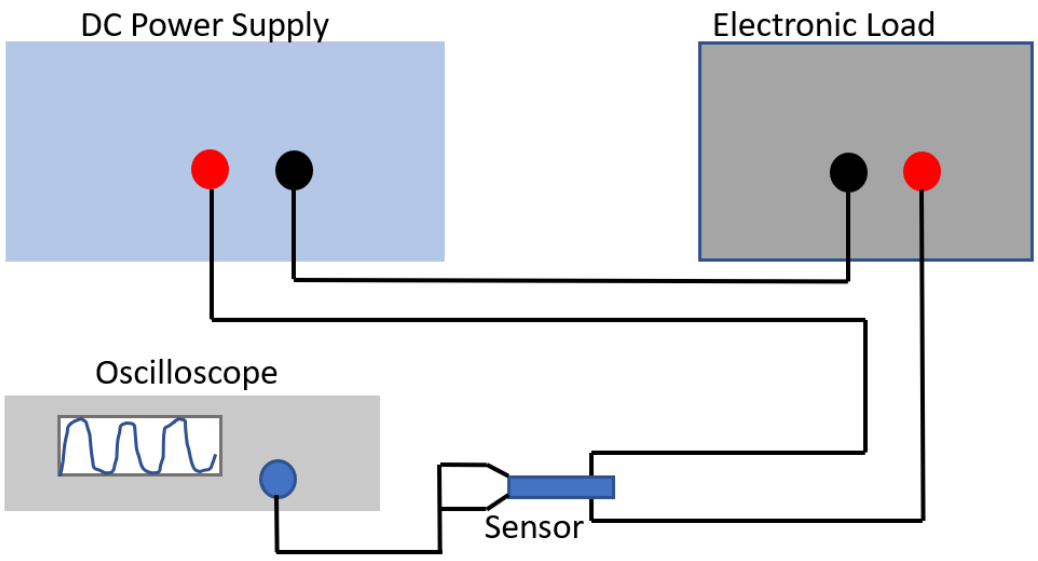

Figure 3. 9: AC Setup Schematic

3.2.3 AC to DC Comparison

The output voltages obtained from the alternating current setup are recorded and compared to those produced by the pulsed direct current setup. The maximum amperage produced by the alternating current setup was not enough to conduct a thorough experiment. Making a conclusion based off the 5 A that the alternating current setup was able to produce is possible, but the assumption that the trend observed would continue up to 30 A would have to be made. The direct current setup was able to produce 30 A which is a more reasonable comparison to amperages observed in the grid.

Both setups were utilized to provide a source current to the proposed sensor and the results show that the pulsed DC current produces similar output voltages to that of the AC setup. To confirm the results of the source current comparison two different piezoelectric cantilevers were utilized. They both showed that the output voltages produce by each setup are very close to one another. The error produced by using a pulsed DC current is negligible for this study. Fig. (3.10) and (3.11) below show the open-source voltage outputs for two different piezoelectric cantilevers using both AC and DC source currents.

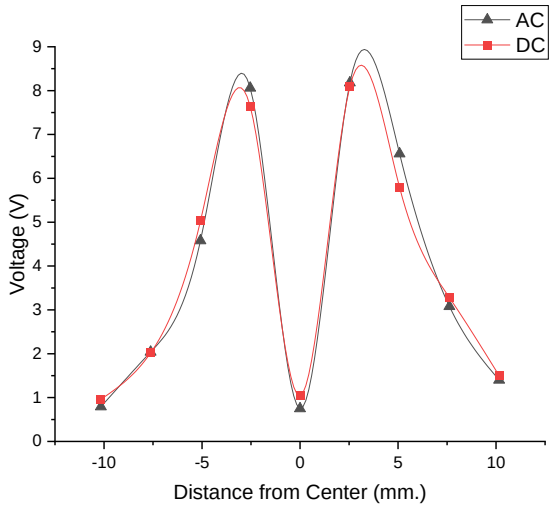

Figure 3. 10: Cantilever 1 Output Voltage for DC and AC Setups

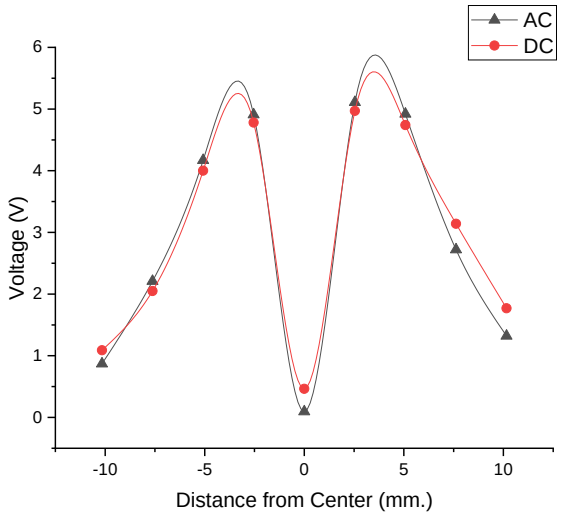

Figure 3. 11: Cantilever 2 Output Voltage for DC and AC Setups

The impedance of each cantilever used was matched with a variable potentiometer which was set to produce maximum power output for the devices. The potentiometer was wired in series with the cantilever with the use of a solderless breadboard kit. This configuration enables quick changes in the power circuit which will be used to store power soon. The impedances of the potentiometers used in this

experiment range from 20 kΩ to 500 kΩ. Fig. (3.12) below shows how the potentiometer was wired to the cantilever and to the oscilloscope used to capture the output voltage.

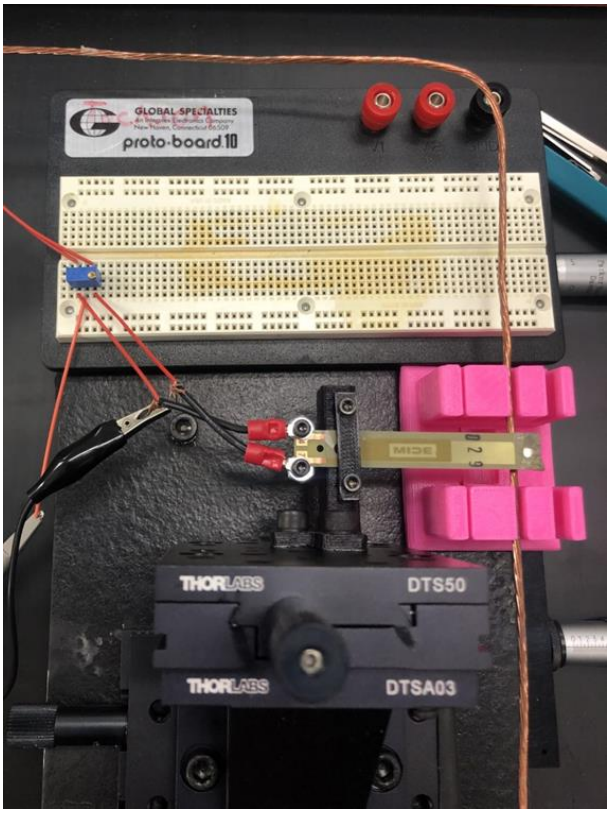

Figure 3. 12: Power Circuit

3.3 Cantilever Comparison

The current sensors resolution and energy harvesting capabilities are dependent on the mechanical properties of the piezoelectric bimorph cantilever. Mechanical properties like stiffness are determined by the materials that make up the cantilever and the overall dimensions of the device. There are many different types of materials that can be used to create the structural portion of the transducer. In previous studies bimorph cantilevers have been made of copper beryllium alloy (Yeh et al., 2021), brass (Lao et al., 2014), and nickel (Ghodsi et al., 2019). These variations in substrate material can cause uncertainty in the reproduction of the study. To improve reproducibility of the results in

this experiment the cantilevers utilized in the sensor are commercially produced by Mide. There were 7 different bimorph cantilevers that were considered for the sensing/harvesting element.

They all utilize FR4 as a structural layer which provides the cantilever with most of its mechanical properties like stiffness and natural resonant frequency. FR4 is commonly used as substrate in printed circuit boards. It is a woven glass reinforced epoxy resin composite which insulates the copper layers used as electrodes from one another. The downside of the material is that it will deform or degrade in the presence of extreme heat over time.

All bimorph cantilevers considered for this application utilize lead zirconate titanate (PZT) as the piezoelectric material. The manufacturer produces a few different types of PZT's with varying material properties. The cantilevers selected contain either PSI-5H4E (PZT 5H) or PSI-5J1E (PZT 5J). PZT 5H has a higher displacement per volt sensitivity than the 5J variant but is more sensitive to temperature changes. According to the manufacturer piezoelectric coefficients can experience up to a 50 percent deviation near temperatures of 150 ℃ in PZT 5H. PZT 5J is more stable at higher temperatures due to its higher curie temperature.

The cantilevers have different overall dimensions. The thickness is directly proportional to the number of piezoelectric layers in each transducer and to the spring constant. For every piezoelectric layer in the device, there are two layers of copper which are used as electrodes. The number of piezoelectric layers ranges from one to four in the cantilevers under consideration. The dimension of the footprint (length x width) of each cantilever is shown in the table below. Because the thickness of each device is

proportional to the number of layers this dimension is omitted from the Table (3.1), but the spring constant is included.

Table 3. 1: Bimorph Piezoelectric Cantilever Selection

Serial Number	Dimmensions (mm)	Spring Constant (N/mm)	# PZT Layers	PZT Type
s452-j1fr-1808xb	71 x 25.4	2.1	4	5J
s230-j1fr-1808xb	71 x 25.4	0.851	2	5J
s234-h5fr-1803xb	71 x 10.3	0.522	2	5H
s233-h5fr-1107xb	53 x 20.8	0.948	2	5H
s128-j1fr-1808yb	71 x 25.4	0.306	1	5J
s128-h5fr-1107yb	53 x 20.8	0.474	1	5H
s129-h5fr-1803yb	71 x 10.3	0.261	1	5H

The cantilevers are all tested for maximum open-source output voltage to determine which will have the highest sensitivity and energy harvesting capabilities. Before testing the devices, they must be tuned to have the natural resonant frequency of 60 Hz. This is because main AC current is generally supplied at 60 Hz in North America. Previous studies have shown that tuning the cantilever to operate at resonance can significantly increase the displacement of the tip of the cantilever beam (Olszewski et al., 2014). This larger displacement results in more power produced by the device.

These bimorph cantilevers were all tuned on a Labworks ET-139 vibration shaker, with acceleration feedback control. The frequency was swept from 20-250 Hz at an acceleration of .1 g's. The cantilevers voltage outputs were monitored with an oscilloscope and the maximum open-source output voltage. Because all bimorph cantilevers had a resonant frequency higher than 60 Hz, a proof mass was added to the cantilevers to reduce the frequency. Due to the different spring constants and dimensions the mass required to tune each device varies. The experimental setup required used to tune the cantilevers is depicted in Fig. (3.13)

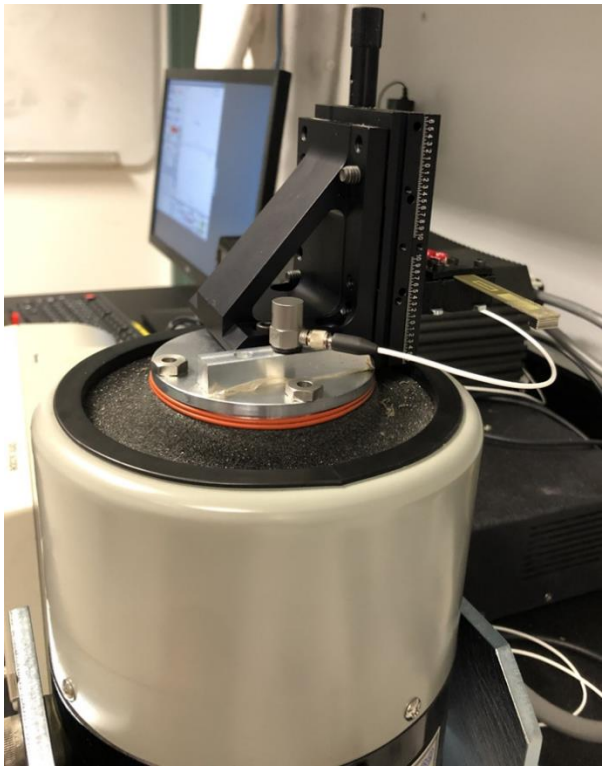

Figure 3. 13: Custom-Made Setup for Resonant Frequency Detection

Neodymium iron boron magnets were selected as the proof mass and were placed on the tip of the cantilever. This location was chosen because the maximum amount of torque on the cantilever is produced forces exerted at the farthest location from the anchor. Increasing the torque on the cantilever will result in higher deflection. The permanent NdFeB-based magnets are thin rectangular prisms and have dimensions of 9.5 x 4.76 x 0.8 mm. After weighing a sample lot of magnets, an average mass of .276 grams was calculated. Magnets were added and removed until the resonant frequency was 60 Hz. The choice of the type of magnet was made based off the remanence. A high remanence manet should be chosen to maximize the coupling force produced with the current's magnetic field. Another good option would have been samarium cobalt magnets. Neodymium produces a much stronger magnetic field but are more sensitive to

temperature changes. For this application the temperature will not reach temperatures high enough for this to matter.

Once all seven cantilevers were tuned to the desired frequency they were tested on the custom experimental setup. The placement of the magnetic proof mass was the same for all trials that were conducted to compare cantilever's open-source output voltage. The source current was set at 25A which is near the maximum amperage attainable by the electronic setup. The 10 AWG conductor which produced the highest magnetic flux density in the computational analysis was utilized for this comparison. The results are plotted in Fig. (3.14).

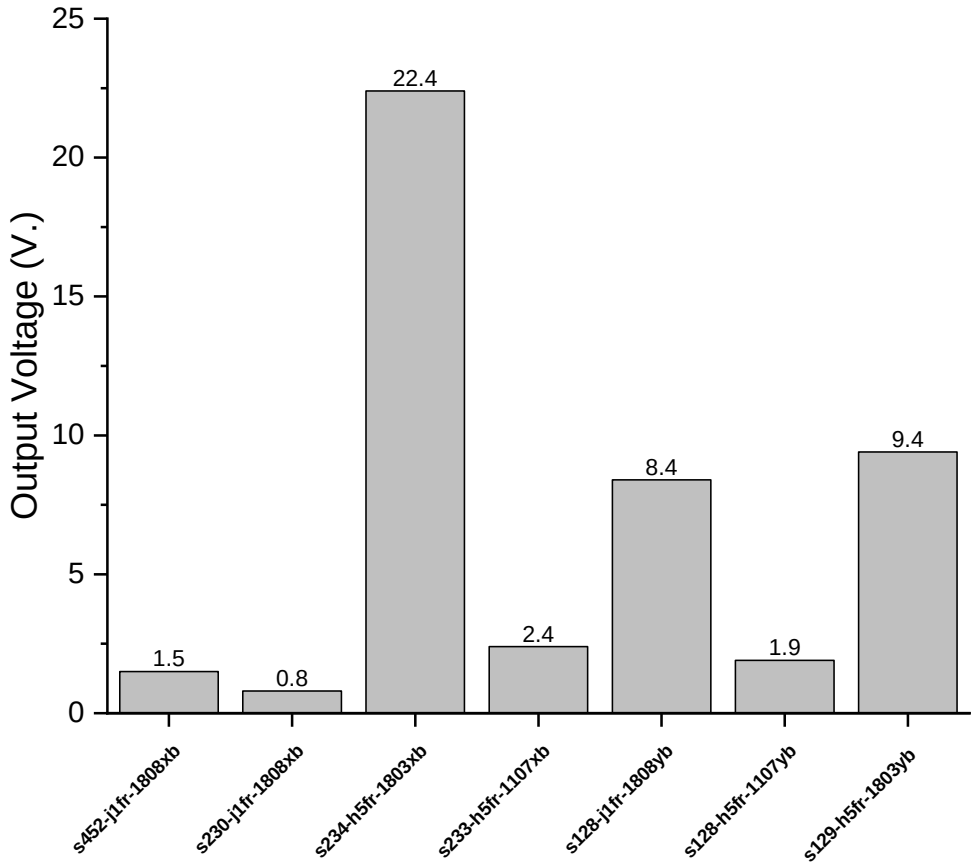

Figure 3. 14: Cantilever Output Voltages at 25A

The cantilever with the maximum output voltage was S234-H5FR-1803XB with a voltage of 22.4 V. The device has two layers of PZT which is the main reason for difference in values when compared to the other seven. The cantilever with four layers (S452) was worth analyzing due to the possibility of large output voltages but the stiffness of the beam proved to be too high. Source current flowing in the conductor did not produce a strong enough magnetic field to induce a substantial force on the end of the cantilever. With a higher source current, the cantilever would experience greater deflections and would produce more voltage, but this could not be verified experimentally in this study. Cantilever S234 is 75.2% less stiff than S452, which allowed for greater deflections in the cantilever.

The dimensions of S234 are 71 x 10.3 mm making this cantilever the longest and most narrow. The second highest output voltage was 9.4 V produced by cantilever S129-H5FR-1803YB, which has the same footprint dimension as S234. Both cantilevers piezoelectric layers are composed of the PZT-5H compound which is ideal for a conducting a comparison of the two transducers. Both cantilevers have the same length, width, and clamping locations which are depicted in Fig. (3.15). The effective length of each cantilever is 51.23 mm once they are placed in the fixture that holds them.

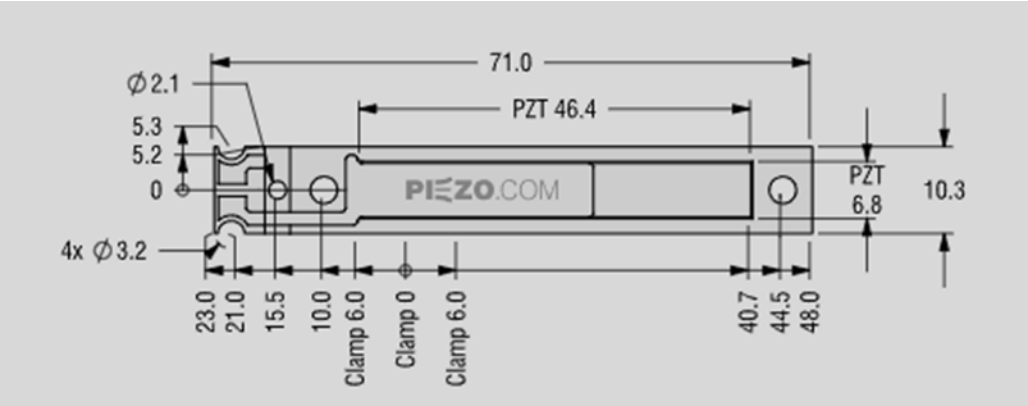

Figure 3. 15: Cantilever Footprint Dimensions (from https://piezo.com)

Based on the data collected of the open-source voltage and cantilever specifications, devices S234-H5FR-1803XB and S129-H5FR-1803YB were selected to be further analyzed as possible sensing elements for the AC current and frequency sensor. The design parameters that are the same in each device is the footprint dimensions (71 x 10.3 mm) and the piezoelectric compound. The differences are in the cantilevers spring constants and overall thicknesses which are outlined in the Fig. (3.16) and Fig. (3.17) below.

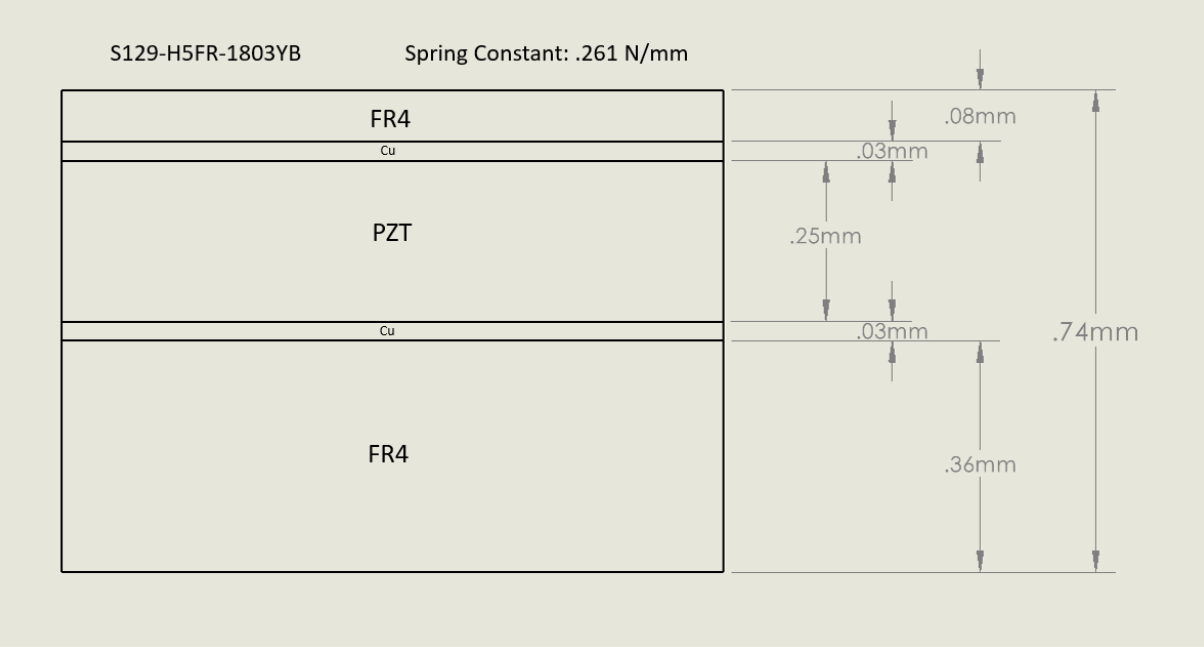

Figure 3. 16: S129 Single Piezoelectric Cantilever Layer Thicknesses

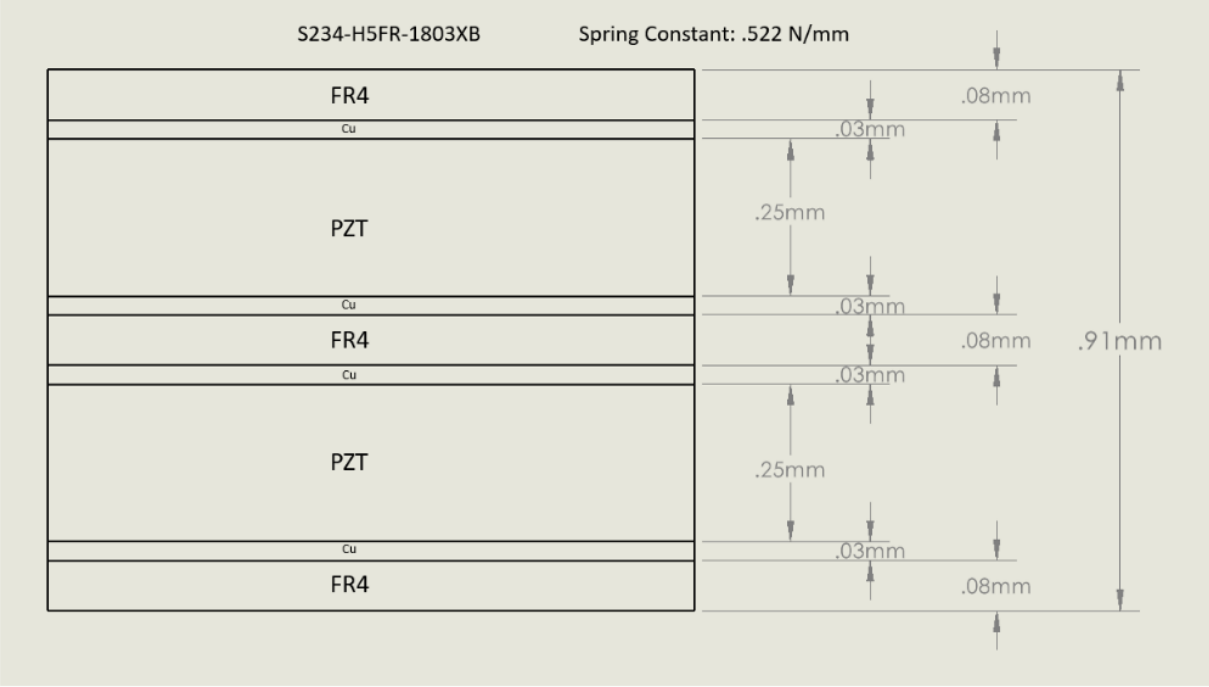

Figure 3. 17: S234 Double Piezoelectric Cantilever Layer Thicknesses

The natural resonant frequency of each cantilever with no mass added is measured to be 141 Hz for cantilever S129 and 170 Hz for the stiffer S234 cantilever. Both cantilevers were tuned with a proof mass made entirely out of magnetic material to perform the initial comparison but were re-tuned once the selection was made.

To better tune the cantilevers to a resonant frequency of precisely 60 Hz, a passive proof mass was utilized along with the hard magnets. These passive proof masses were small pieces of silicon in the shape of a rectangular prism. Various combinations of passive and magnetic proof masses were used to tune each cantilever. The use of different combination of proof masses provided the opportunity to analyze the effect of the pull strength of the magnetic proof mass. A single magnet showed to have the pull strength of 2.94 N. The response in output voltage and in the operational bandwidth of the sensor was analyzed for each combination.

The proof mass that achieved a resonant frequency of 60 Hz was weighed to determine the required mass to achieve target resonant frequency. The same amount of passive mass added to the cantilever was subtracted from the magnetic mass to maintain the desired total mass. This was done to maintain the natural resonant frequency of 60 Hz.

The proof masses utilized in this study are a purely magnetic proof mass, a proof mass with a magnet thickness of 2.4 mm, and a proof mass with a magnet thickness of 0.8 mm. Due to the different stiffnesses in each cantilever, the total mass needed to achieve the desired resonant frequency was different in each case. Table (3.2) below describes each scenario and the amount of each type of proof mass used to achieve 60 Hz.

Table 3. 2: Passive and Magnetic Proof Mass Combinations

Cantilever	Magnet Thickness (mm.)	Magnetic Mass (g.)	Passive Mass (g.)	Total Mass (g.)
S129	3.2	0.913	0	0.913
S234	5.6	1.687	0	1.687
S129	2.4	0.83	0.098	0.928
S234	2.4	0.83	0.8525	1.6825
S129	0.8	0.276	0.647	0.923
S234	0.8	0.276	1.41	1.686

Chapter 4: Sensor Characterization

The zero-power AC current sensor proposed in this study can detect fluctuations in current amplitude and frequency. There are many design parameters that impact the sensor's ability to detect currents and harvest energy. This study investigates a few of these design parameters including the effect conductor type has on the sensor's overall performance. Another parameter investigated is the effect cantilever mechanical properties have on the optimal placement of the cantilever, power generation, and operational bandwidth.

In this section the resolution of the sensor is determined for both stranded and solid conductor types. The bandwidth of the device is determined by varying the frequency of the source current. Using a combination of passive and magnetic proof masses the bandwidth is adjusted for different applications.

4.1 Spatial Optimization

The spatial positioning of the magnetic proof mass with respect to the current carrying conductor is a critical design parameter of the sensor. The relative position of the cantilever is crucial in both sensing and energy harvesting applications because it determines the electromagnetic forces that act on the magnet. This means the position of the cantilever indirectly determines the sensitivity and the power generation capabilities of the sensor.

4.1.1 Previous Spatial Optimization Studies

In earlier studies conducted by the researchers who founded this concept the optimal position for a single bare conductor was where the magnetization vector of the magnet (in the vertical direction) and the radial position vector make a 45° angle (Leland et al.,

2010) (Leland et al., 2009) (Leland, n.d.). The conclusion assumed that only the vertical component of the force produced by the magnetic field needs to be accounted for. Many other researchers who developed energy harvesters/current sensors accepted this theory as true (Isagawa et al., 2011) (Suzuki et al., 2013) (Xu et al., 2013). Upon the analysis of experimental data collected, it was found that the theory of an optimal position at a 45° angle for a single wire conductor did not hold true for all circumstances. Researchers showed that the data did not match the theory presented by Leland et al. and the reason being that other forces that act on the cantilever were assumed to be negligible (Houlihan et al., 2016) (Houlihan et al., 2019).

4.1.2 Spatial Optimization Based on Cantilever Properties

For the experimental portion of this study, we can conclude that the optimal position of the magnetic proof mass is dependent on the diameter of the conductor and the stiffness of the cantilever. The experimental data agrees with the simulation discussed in chapter 2 of this thesis. The voltage produced by each cantilever at a constant source current of 15 A is greater for the solid conductor than for the stranded of the same gauge. The output voltage of each cantilever is plotted against the distance from the center of the conductor in each plot shown below. Fig. (4.1) shows the data collected for the 10 AWG solid conductor which had the highest output voltages for both cantilevers. Cantilever S234 had a voltage output of 13.04 V with an optimal placement of x = -3.175 mm and S129 produced 8.78 V at x = -2.54 mm. The COMSOL Multiphysics model predicted an optimal placement of x = -3.175 mm which is in an acceptable range for this gauge of conductor.

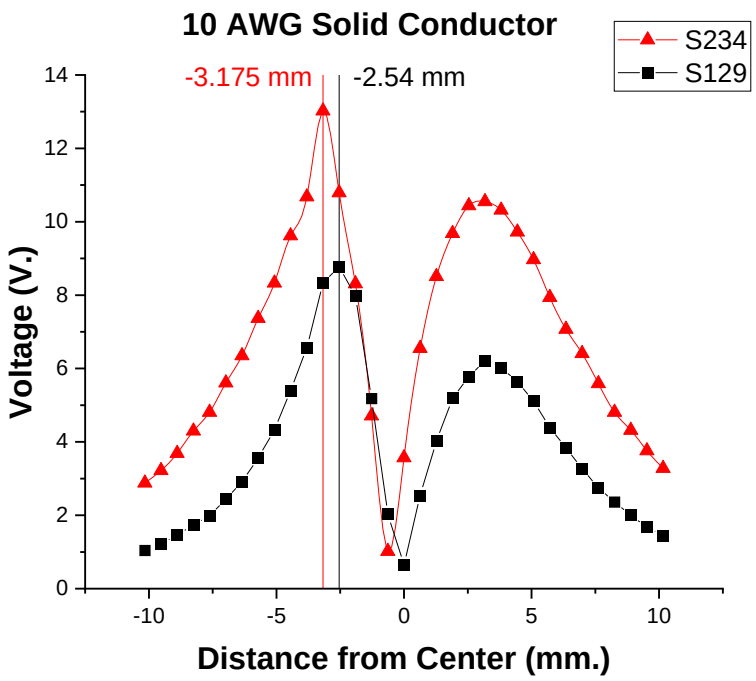

Figure 4. 1: Optimal Magnet Placement for 10 AWG Solid Conductor

The output voltages recorded for the stranded 10 AWG conductor for S234 is 12.34 V and 7.6 V for S129. The optimal placement of the cantilever is the same as that recorded for the solid conductor. The output voltages of both cantilevers are plotted against the distance to the center for the stranded conductors in Fig. (4.2).

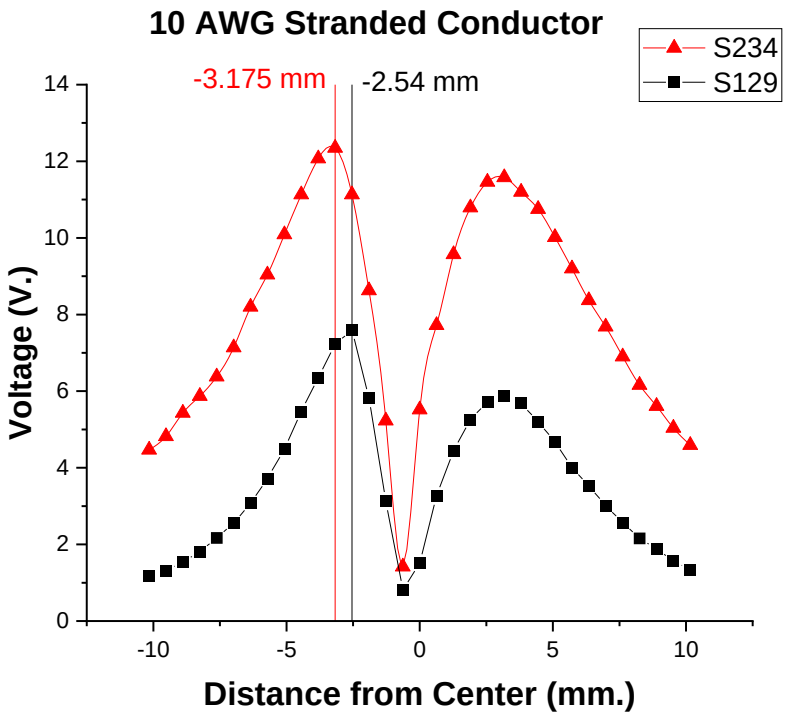

Figure 4. 2: Optimal Magnet Placement for 10 AWG Stranded Conductor

The optimal angle of the magnet with respect to the conductor for both conductor types are represented by the angle θ. The angle is defined with the magnetization vector of the magnet and the radial vector with the center of the conductor. The magnetization vector is placed at the center of the conductor and points in the positive y direction as shown in Fig. (2.16). The angle reported in this study produces maximum coupling effects between the current produced cantilever and the magnetic field of the proof mass.

For the 10 AWG conductors' the optimal angle for each cantilever is $\theta = 33.97^{\circ}$ for S129 and 40.1° for S234.The optimal angle is determined for different gauge conductors. This is done the same way as with the 10 AWG conductor.

The optimal placement is determined experimentally for 8 AWG solid and stranded conductors. For cantilever S234 the optimal placement is at x = -3.81 mm which produces an angle of $\theta = 45.3^{\circ}$. For S129 optimal placement is at x = -3.175 mm which

corresponds to an angle of θ = 40.1° for S129. Optimal placement is the same for both conductor types but have different voltages. The output voltage produced by the solid conductor is shown in Fig. (4.3). The maximum voltage output of cantilever S234 is 10.56 V while S129 had a maximum of 4.66 V.

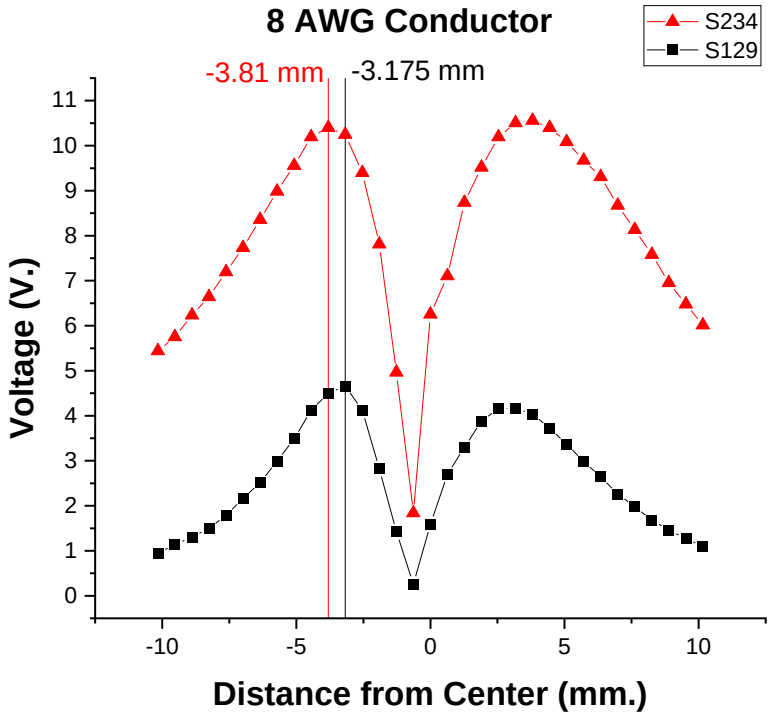

Figure 4. 3: Optimal Magnet Placement for 8 AWG Conductors

For cantilever S234 the optimal placement is at x = -4.45 mm which produces an angle of θ = 49.73° and x = -3.81 mm for S129 which produces an angle of θ = 45.3° as mentioned previously. Just as observed in the previous case cantilever S234 has a higher output voltage of 8.69 V while S129 produced a maximum of 2.97 V and is plotted in Fig. (4.4) below.

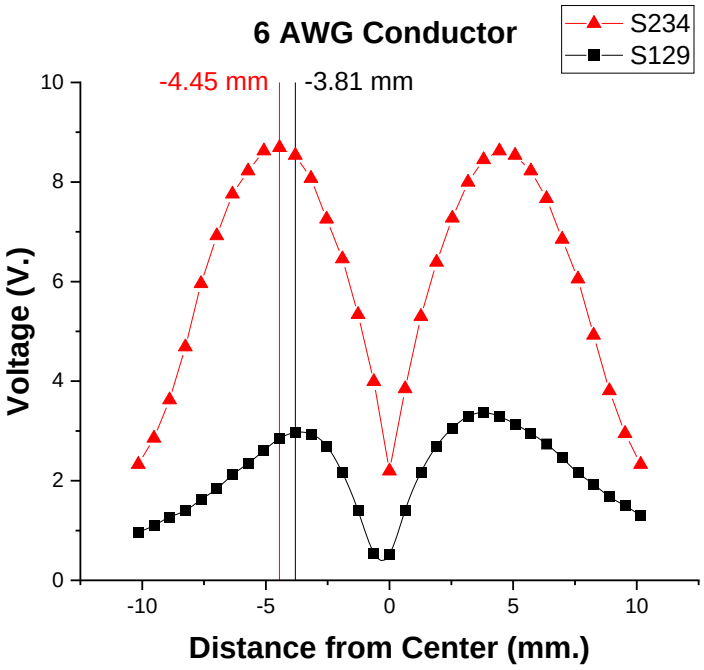

Figure 4. 4: Optimal Magnet Placement for 6 AWG Conductors

4.1.3 Spatial Optimization Conclusion

The relative position of the cantilever is crucial to the performance of the sensor. In this section of this study the optimal position of each cantilever is reported for each gauge of wire analyzed. Cantilever S234 is stiffer than S129 due to more layers. The stiffer cantilever needs to be farther from the center of the conductor to produce maximum output voltages for all cases. The single layer cantilever S129 has a maximum output at a closer location to the center of the conductor. Smaller gauges of conductors have a greater optimal distance than the larger gauges. The optimal positioning is independent of conductor type as the results in this study only varied for cantilever stiffness and conductor gauge. Fig. (4.5) below depicts the optimal placement of each scenario tested and is not to scale.

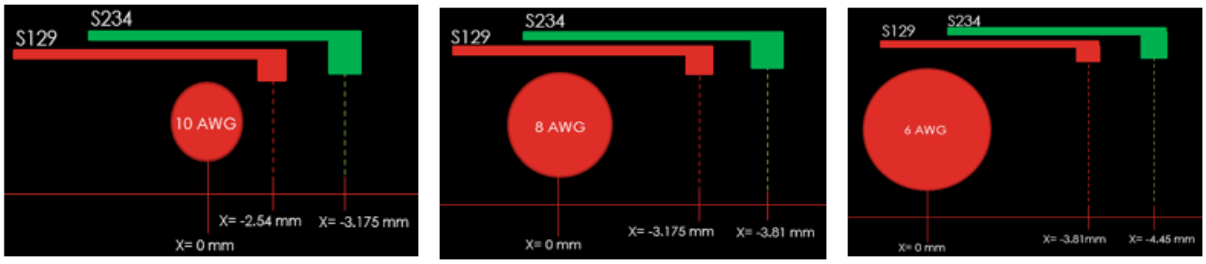

Figure 4. 5: Schematic of Optimal Magnet Placement for All Gauges

Although the optimal positioning of the cantilever did not vary for the different conductor types utilized in this study, the magnitude of the output voltage did. The cantilevers were placed at the respective x-coordinate according to wire gauge for output voltage testing. For every experimental scenario conducted in this study the solid conductor produced a higher output voltage than the stranded. This result agrees well with the simulation conducted on the coupling between the magnetic proof mass and the magnetic field produced by the current carrying conductor. Table (4.1) and (4.2) below show the experimental results obtained from the study.

Table 4. 1: Output Voltage for All Gauges of Solid Conductors

	Solid Conductor		
Cantilever	**10 AWG Output (V.)**	**8 AWG Output (V.)**	**6 AWG Output (V.)**
S129	8.78	4.66	2.97
S234	13.04	10.56	8.69

Table 4. 2: Output Voltage for All Gauges of Stranded Conductors

	Stranded Conductor		
Cantilever	**10 AWG Output (V.)**	**8 AWG Output (V.)**	**6 AWG Output (V.)**
S129	7.6	4.52	2.44
S234	12.34	8.64	6.71

4.2 Sensor Current Resolution

The different design parameters for the cantilevers analyzed in this study demonstrate the importance of carefully selecting certain mechanical properties to optimize the sensors performance. Cantilever S129 has one piezoelectric layer and a smaller spring constant meaning that it can more easily detect changes in the frequency of the source current. Cantilever S234 has two piezoelectric layers and is 2 times stiffer. The larger spring constant means a greater magnitude force is required to generate large displacements. The two piezoelectric layers make the cantilever have a higher power density than S129. The stiffer cantilever requires more magnetic mass to be added to reach a resonant frequency of 60 Hz. The larger magnetic proof mass will produce more force when magnetically coupled to the current generated magnetic field.

The open-source voltage is recorded for both cantilevers and plotted versus the source current to determine the resolution each cantilever can provide. The custom electronic setup is utilized to produce a source current that ranges from 0-30 A. The 10 AWG solid conductor was utilized for the sensitivity analysis because of the high output voltages produced in the previous section. The source current was incremented in smaller values to determine the sensor resolution and is shown in the inset figure in each plot. The inset shows a higher resolution x-axis of .1 A over a 2 A range.

The single layer cantilever, S129, has a maximum output voltage of 11.6 V for the solid conductor and a slightly lesser 11.25 V for the stranded conductor. The cantilever has a steeper slope for the solid conductor at .55 V/A compared to the stranded conductor which is 0.40 V/A. The electrical noise recorded for the experimental setup ranges from 6-10 mV. Due to the limitations imposed by the noise the minimum detectable change in

current is 18.2 mA for the solid conductor and 25 mA for the stranded. This shows that the solid conductor provides both a higher output voltage and current resolution for cantilever S129. The output voltage of S129 is plotted versus the source current for both conductor types in Fig. (4.6) shown below. The voltage output of S129 shows more of a linear trend than that of the double layer cantilever S234.

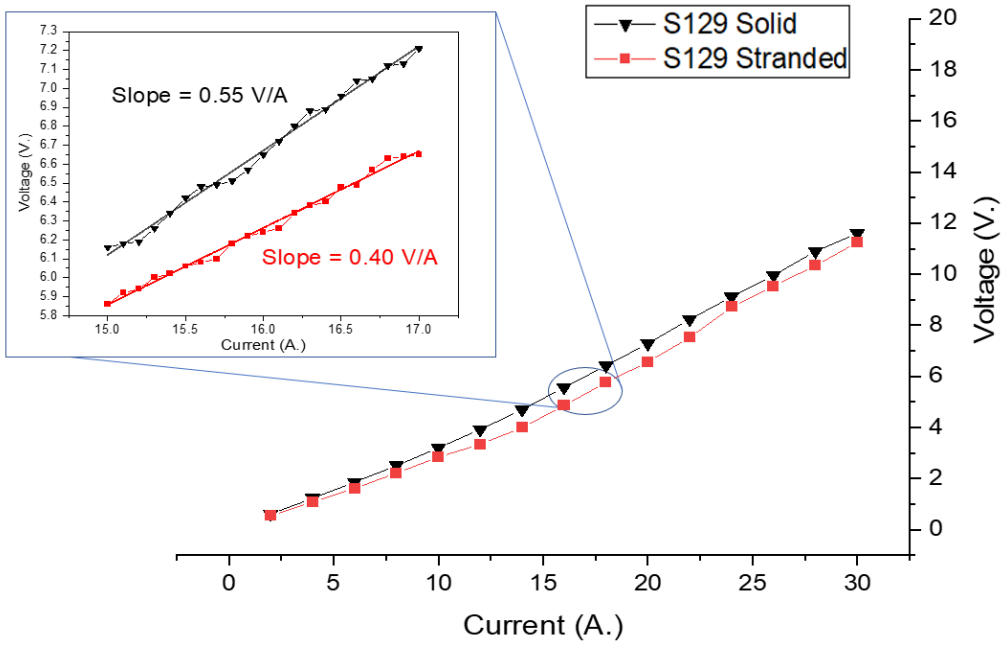

Figure 4. 6: S129 Output Voltage Sensitivity for Both Conductor Types

Cantilever S234 shows a much higher open-source voltage for the same range of source current due to the second layer of piezoelectric material. The maximum voltage observed is 28.05 V from the solid conductor and a lesser 26.26 V for the stranded conductor. The solid conductor combined with cantilever S234 show the largest slope recorded of 1.12 V/A. The stranded conductor has a slope of 0.96 V/A, which is still higher than what the single layer cantilever can produce. The output voltages recorded for each conductor type is shown in Fig. (4.7). Just as before, the noise detected for the setup is 6-10 mV. The minimum detectable change in current is 8.9 mA for a solid conductor

and 10.2 mA for the stranded conductor. These experimental results agree well with what the finite element model predicted. The stranded conductors produce less deflection in the cantilevers due to the smaller coupling forces, which is shown as less magnetic flux density in the computational models.

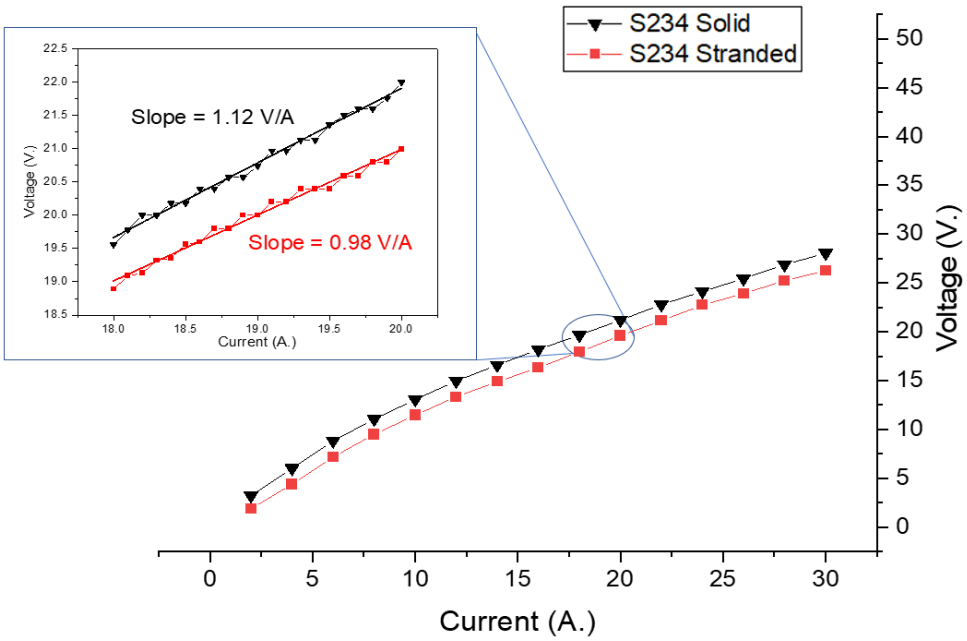

Figure 4. 7: S324 Output Voltage Sensitivity for Both Conductor Types

4.3 Energy Harvester

Harvesting energy from magnetic fields produced by a current carrying conductor has proved to be an efficient and effective method to power wireless sensor nodes. The deployment of these types of sensors can reduce labor spent on maintaining power sources. The previously mentioned power density of each cantilever is of interest when analyzing the energy harvesting capabilities of the sensor.

4.3.1 Impedance Optimization

Both cantilevers were tested with the solid 10 AWG conductors for energy harvesting capabilities. This configuration provides the best-case scenario for the sensor. To achieve

maximum power levels both cantilevers' impedances were matched using variable potentiometers. The variable potentiometers utilized in this study had a range of 20-500 kΩ. The resultant impedance versus power graphs shown below demonstrate that both cantilevers have a peak power at 200 kΩ. Each cantilever was tested with a source current of 10 and 20 A to ensure the resistance selected was optimal for the entire source current range. For Cantilever S129, the maximum power produced is .43 mW at 200 kΩ with a source current of 20 A. The lower source current of 10 A produced a maximum power of .15 mW also at at 200 kΩ. Taking into consideration the volume of cantilever S129 this results in a power density of 1.086 mW cm^{-3} at 20 A.

For cantilever S234 a much higher 2.58 mW of power was produced from the 20 A source current at 200 kΩ. The 10 A source current produced a maximum of 1.1 mW at 200 kΩ as well. It is evident from the figures that above 200 kΩ the power produced by both cantilevers is reduced dramatically. The power density produced at 20 A for cantilever S234 is 5.69 mW cm^{-3}.

The reduction in power is more evident at high currents but is still present for the lower source current trials. The 200 kΩ potentiometer was utilized in all power experiments based on Fig. (4.8).

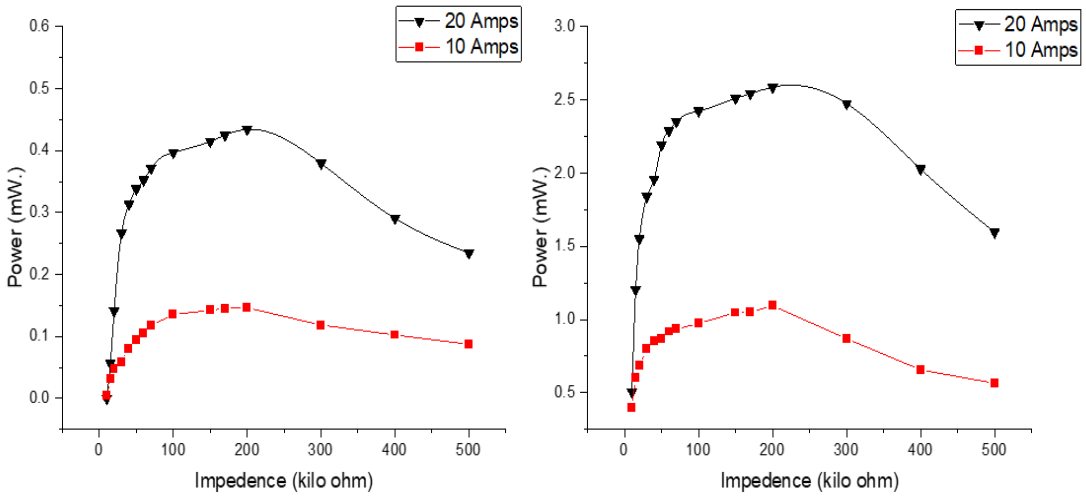

Figure 4. 8: Power versus impedance for (left) S129 and (right) S234 with varying current and load impedance.

4.3.2 Power Generation

A design requirement of this device is to be self-sufficient so the energy harvesting capabilities of each one of the cantilevers was analyzed. For this experiment, the 10 AWG conductors are utilized as this gauge has the strongest magnetic coupling with the proof mass. The cantilevers were positioned in the optimal location according to results from the previous section. The source current was increased to 30 A in 1 A increments and the power produced from each cantilever was recorded. These figures tell us how the device harvesting capabilities will be affected when changes in the source current occur as well as the maximum power produced at 30A. Cantilever S129 produced a maximum of 0.67 mW (1.69 mW cm^{-3}) with the solid conductor and a lesser power .63 mW (1.59 mW cm^{-3}) with the stranded. Just as the open-source voltage figures showed, the resolution observed for the solid conductor is higher than that of the stranded. Fig. (4.9) below shows the power produced plotted against the source current.

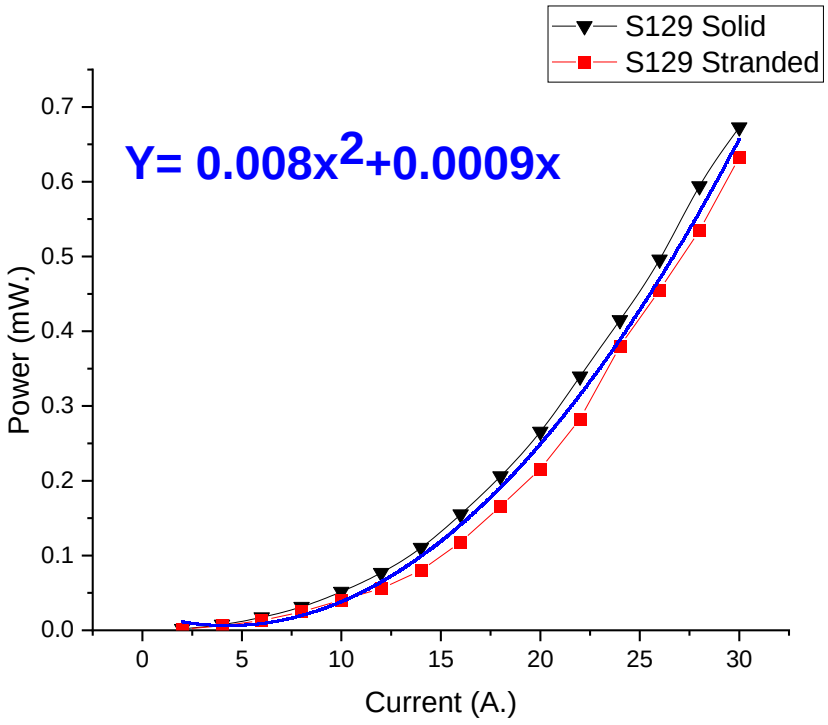

Figure 4. 9: S129 Power Sensitivity for Both Conductor Types

Cantilever S234 produced more power with both conductor configurations than the single layer cantilever S129. Although cantilever S234 has double the amount of piezoelectric material, the power is more than double of the levels observed for cantilever S129. The maximum power output is produced by the solid conductor and has a magnitude of 3.66 mW (8.06 mW cm^{-3}). The stranded conductor has a magnitude of 3.44 mW/A (7.58 mW cm^{-3}). The power produced by S234 with a solid and stranded conductor are plotted in Fig. (4.10). Using power fitting we were able to develop equations to accurately predict power output as a function of current for both plots. This amount of power is enough to power a wireless sensor node which typically uses about 100 μW (Paprotny et al., 2013).

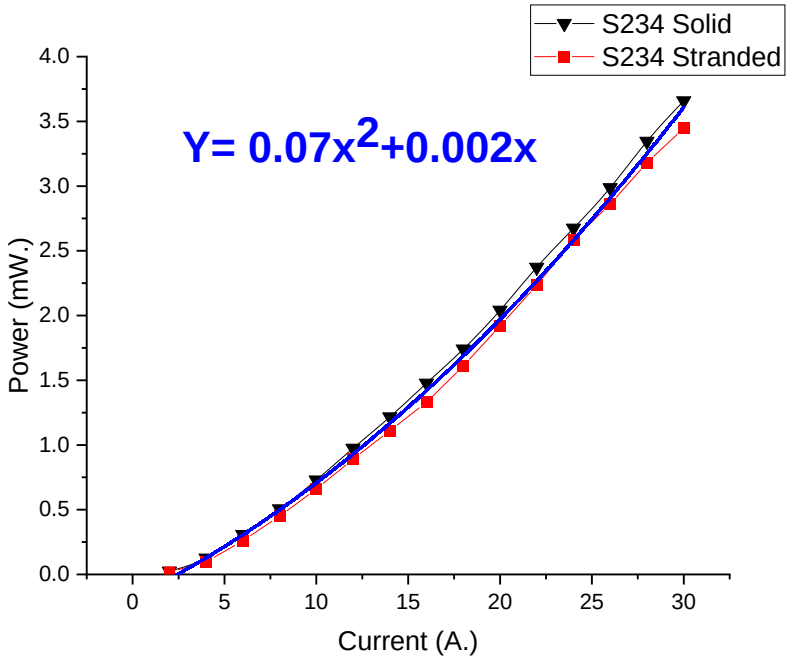

Figure 4. 10: S234 Power Sensitivity for Both Conductor Types

4.4 Frequency Response

The proposed zero-power sensor can measure the amount of current flowing through a conductor as well the frequency at which the alternating current is oscillating. Sensing the frequency in the grid is important because a slight deviation from the target frequency can cause damage to many infrastructures and be a threat to national security. A large enough change in frequency can cause protection systems to go down and cause a collapse of the electrical grid.

4.4.1 Frequency Resolution

The frequency of the output voltage produced by the sensor is a result of the changing magnetic field produced by the alternating current in the conductor being monitored. The change in the direction of the magnetic field produced by the conductor is due to the changing direction of electric potential. This change in direction is what causes the

deflections in the cantilever. The cantilever can detect the number of times the direction of the magnetic field changes which is also the frequency of the current. The oscillations per second of the cantilever is dependent on the frequency of the AC current.

The open-source output voltage of the sensor is plotted against time in Fig. (4.11a). This output voltage is for a source current with a frequency of 60 Hz and with cantilever S234 as the sensing element. The cantilever was selected for this trial because the two-layer piezoelectric cantilever showed higher resolution than the single layer one. The frequency of the output voltage is further demonstrated with a closer view of the sine wave which is shown in Fig. (4.11b) which shows 6 peaks for a time interval of 0.1 s. The theoretical frequency was determined using the pulse width of the electronic load in seconds because it is what is simulating the alternating current. Equation (15) is what was used to determine the theoretical frequency and Equation (16) is used to determine the error.

$$F_{Theoretical} = \frac{1}{2 \times t} \qquad (15)$$

$$Error = \left(\frac{F_{Measured} - F_{Theoretical}}{F_{Theoretical}}\right) \times 100\% \qquad (16)$$

At 60 Hz, the resonant frequency of the cantilever, the frequency measured by the sensor had an error of 0.003%. The number of peaks were counted for different source current frequencies, and this was the measured frequency provided by the sensor. The theoretical frequency was determined using equation (15) and the error for each case was then calculated with equation (16). Fig. (4.11c) demonstrates that for frequencies that are much lower than the natural resonant frequency of the cantilever error is very high. The 60 Hz resonant frequency and driving frequency combine at lower frequencies which causes more peaks in the output voltage. For example, if the source current is at 10 Hz

that means a force on the cantilever would occur every 0.1 s but the force would cause the cantilever to resonate after the force was applied. Therefore, if the wave peaks are counted there could be several false peaks causing an increase in the error. Although the error is observed at these low frequencies is extremely high, the frequency in the electrical grid does not vary by more than 1 Hz on the regular so this should not affect the accuracy of the sensor. The error of the frequency measured by the sensor for frequencies near 60 Hz is shown in Fig. (4.11d) and show that the error increases as the source current deviates from the resonant frequency.

The sensor can detect changes of less than 0.1 Hz but because the method used to determine the measured frequency has a maximum resolution of 0.1 Hz, smaller deviation could not be investigated.

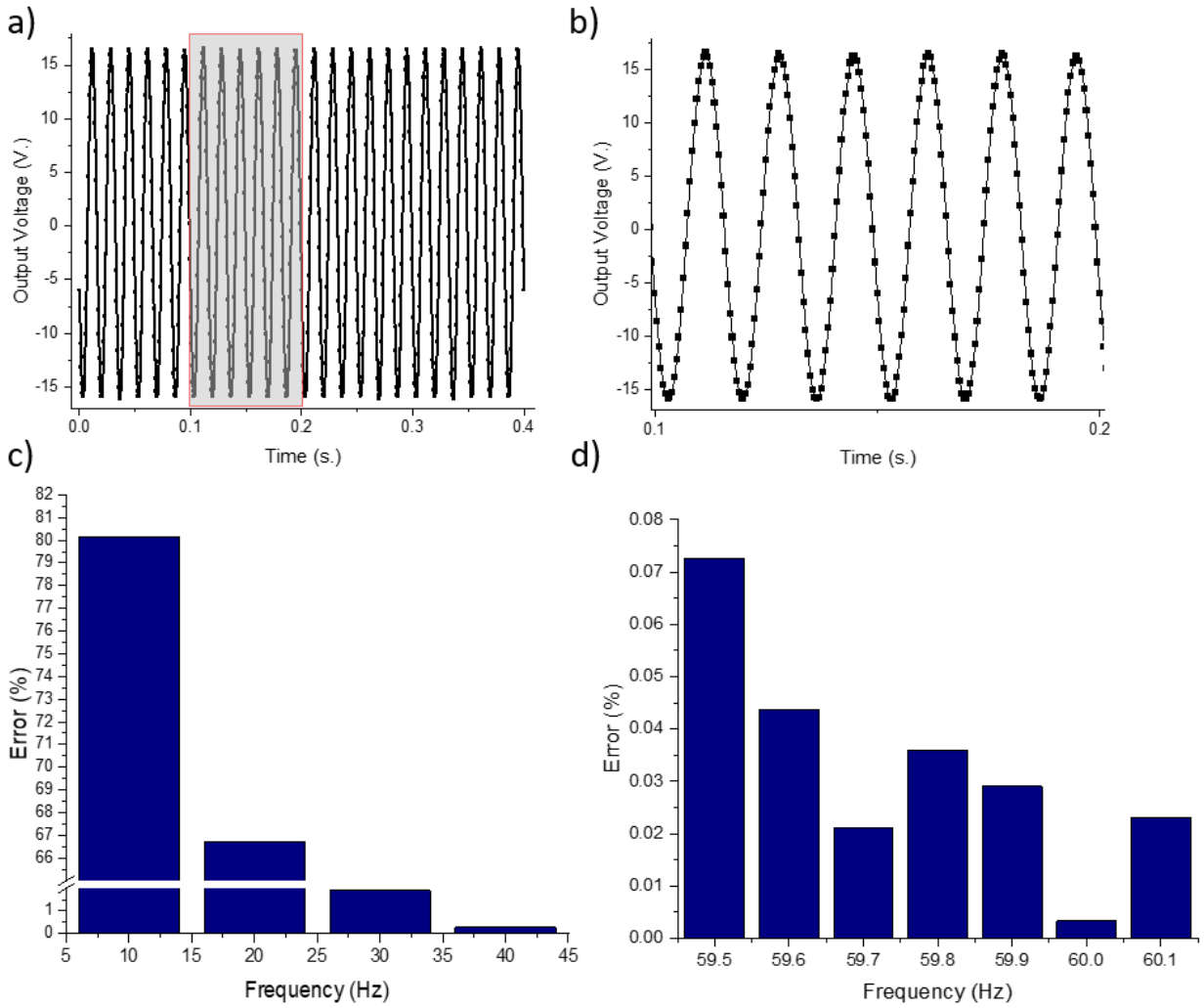

Figure 4. 11: (a) Output voltage versus time for 60 Hz source current (b) 0.1 second window of output voltage versus time for 60 Hz source current. Detection error for (c) a variety of source current frequencies (d) and near resonant frequency

4.4.2 Magnetic and Passive Proof Mass

The effects of combing a passive and magnetic proof mass to tune the cantilevers resonant frequency have been analysed in this study. The use of a passive proof mass can optimize sensor performance for specific applications. A high Q-factor is a well-known characteristic of cantilevers. This can limit the applications for a device that utilizes a cantilever as a sensing element. Sensing current in a conductor requires a relatively small bandwidth, but as mentioned before small fluctuations are observed in some cases and can be detrimental to equipment and systems. For the application of this device a high Q-

factor is desirable for increased energy harvesting capabilities and sensitivity. In some scenarios it may be necessary to widen the bandwidth of the sensor.

One technique to widen the bandwidth of this sensor is to remove a portion of the magnetic proof mass and add a passive mass to obtain the desired resonant frequency. This theory was demonstrated by testing different ratios of magnetic to passive proof mass. Due to limitations of the magnets physical dimensions the scenarios analysed are tuning the cantilever with a proof mass composed of magnets entirely, a magnet thickness of 2.4 mm along with a passive proof mass, and a magnet thickness of 0.8 mm along with passive proof mass. Because the pull strength of the magnet is linearly related to the thickness of the magnets, these combinations resulted in 8.82 N and 11.76 N respectively.

The amount of passive proof mass added to the cantilever in each case was determined by the target resonant frequency of 60 Hz. The total mass required to bring cantilever S129 to target resonant frequency was approximately .92 grams, while cantilever S234 needed 1.68 grams. To determine the operational bandwidth of the sensor the output voltage was plotted against the frequency of the source current and is shown in Fig. (4.12). The output voltage of each cantilever was made equal to reduce the number of parameters and to not skew the value of the slope on each side of the bell curve produced. This was done by adjusting the source current so that each cantilever produces approximately 13 V. The 10 AWG solid conductor was utilized for this analysis to provide the most magnetic coupling for the reduced amount of magnetic material.

The results of this portion of the study suggest that as pull strength increases a higher output voltage is produced along which increases device sensitivity and energy harvesting capabilities. S129 showed the highest sensitivity to frequency changes with a

purely magnetic proof mass at a slope of 13.18 V/Hz. A higher slope represents a higher Q-factor which is desirable for this device's application. The sensitivity to variations in frequency reduce with the amount of magnetic material on the cantilever. With a 2.4 mm thick magnet the resolution is 12.88 V/Hz and drops to 8.77 V/Hz with a magnet thickness of 0.8 mm.

Cantilever S234 can produce more power but is less sensitive to changes in frequency. Even with a proof mass made entirely of magnetic material the resolution of this cantilever is 8.79 V/Hz. This value is close to the lowest magnetic material trial of cantilever S129, but S234 still produces twice the voltage. With a magnet thickness of 2.4 mm the resolution of S234 is 8.15 V/Hz then drops to 4.30 V/Hz with a magnet thickness of 0.8 mm.

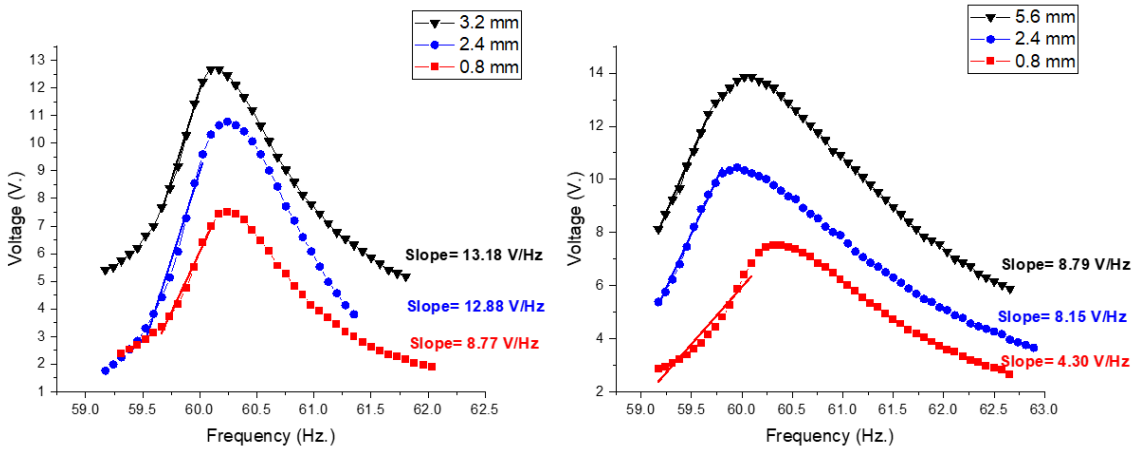

Figure 4. 12: Frequency sensitivity for combinations of passive and magnetic proof mass for (left) S129 and (right) S234

Both cantilevers produce around 7 V of open-source voltage with a magnet thickness of 0.8 mm but cantilever S234 is far less sensitive to changes in frequency. This enables cantilever S234 to provide usable power for a wider frequency range than S129 could provide.

The full width at half maximum (FWHM) of each curve also tells us how the bandwidth of the device has responded to changes in the amount of magnetic proof mass used. The bandwidth recorded for all combinations of passive and magnetic proof masses is smaller for cantilever S129. The FWHM for a magnetic material proof mass with no passive mass is 0.993 Hz. It then increases to 1.19 Hz with a magnet thickness of 2.4 mm and finally 1.23 Hz with a magnet thickness of 0.8 mm. The FWHM is inversely proportional to the amount of magnetic material used.

Cantilever S234 shows the same trend but starts with a larger FWHM and shows a smaller range. For S234 the FWHM for a magnetic material proof mass with no passive mass is 1.71 Hz. It then increases to 1.77 Hz with a magnet thickness of 2.4 mm and finally to 1.81 Hz with a magnet thickness of 0.8 mm.

4.5 Conclusion

Several design parameters have been analyzed for the zero-power AC current sensor proposed in this thesis. This study validated that a single device could be used to harvest energy to power a WSN while obtaining data in regard to current amplitude and frequency. This was the first time that a multifunction device has been demonstrated for smart grid applications using real world stranded wires with high current. The optimization of the placement and mechanical properties of the cantilever were considered as well as the effects of different conductor configurations. This section will summarize the findings of the experiments conducted for this study.

4.5.1 Cantilever Selection

Each cantilever analyzed in this study has certain benefits and drawbacks. The single layer piezoelectric cantilever has a lower spring constant than that of the double

layer device. The smaller spring constant makes the cantilever S129 easier to deflect and has proven to have a higher Q-factor which makes it better at sensing deviation in the current frequency. The drawback of using this cantilever is that the energy harvesting abilities are hindered by the single piezoelectric layer and this device is less sensitive to changes in AC current amplitude.

Cantilever S234 on the other hand has a higher spring constant due to the two piezoelectric layers. It doesn't detect changes in frequency as well as S129 but would still function well as a frequency sensing device. The power produced by S234 is much higher than that of the single layer cantilever and it has higher current sensing resolutions for both stranded and solid conductors. The overall best cantilever for this device is S234.

4.5.2 Conductor Configuration Effects

The magnetic field produced by each type on conductor and the magnetic coupling with the proof mass was computationally analyzed and verified through experimentation. The magnetic field produced by a solid conductor demonstrated to provide more efficient coupling with the magnetic proof mass than the stranded. The better coupling from the solid conductor resulted in more deflection in the cantilevers and more electricity generation in the piezoelectric films. This held true for both cantilevers that were analyzed in this study.

Both conductor types were utilized while determining the cantilevers current amplitude sensing resolution. The cantilevers displayed lower resolutions when sensing current in the stranded conductors. The solid conductor provided higher resolution and current resolutions for all cases.

4.5.3 Optimal Proof Mass Positioning

Experimental results demonstrated that the stiffer cantilever needs to be farther from the center of the conductor to produce maximum output voltages for all gauges of conductor. The single layer cantilever S129 has a maximum output at a closer location to the center of the conductor. Smaller gauges of conductors have a greater optimal distance than the larger gauges. The optimal positioning is independent of conductor type as the results in this study only varied for cantilever stiffness and conductor gauge. Fig. (4.5) demonstrates the conclusion reached with a schematical representation of all scenarios tested.

Chapter 5: Future Works

This thesis proposes a zero-power AC current sensor and the experiments conducted are to optimize design parameters. The study can be continued due to the various design parameters this thesis did not investigate. There are many scenarios that were not considered but are of interest when designing a proximity sensor of this type.

5.1 Conductor Configurations

This study investigated coupling effects for conductors that were both stranded and solid of 10, 8, and 6 AWG. All conductors utilized in this study are made of copper and are non-insulated. Other conductor sizes can be investigated with larger amounts of current to investigate the amount of power produced by different cantilevers. More current flowing through the conductor would produce a greater force on the magnetic proof mass. A cantilever that was not utilized in this study because it is too stiff would be ideal for a very high current application. With a higher current being used, testing conductors with insulation would be possible and of interest.

There are many configurations that were not investigated in this study that are utilized in the electric grid. A typical cable type utilized in the electric grid from power transmission is an aluminum conductor steel reinforced (ACSR) cable. These cables can be modeled using finite element analysis to determine optimal magnetic proof mass placement and then experimentally verified like the conductors analyzed in this study. Fig. (5.1) below shows the stranded conductor configuration that was utilized in the experiments performed for this thesis. Fig (5.2) shows another ACSR conductor configuration that can be analyzed experimentally and with simulations.

Figure 5. 1: Stranded Conductor Utilized in Study

Figure 5. 2: Aluminum Conductor Steel Reinforced Cable

5.2 Magnetic Proof Mass Geometry Optimization

The geometry of the magnetic proof mass is a parameter that effects the overall torque produced on the cantilever. A rectangular prism shaped magnet is what was used for all experiments in this study but a magnet with a different shape could simplify the

positioning of the sensor. A custom-made magnetic proof mass could reduce the error associated with the cantilevers position with respect to the conductor.

The simulations performed for this study were all 2-dimmensional but a 3-dimmensional study could be useful when analyzing different geometries. For instance, a cylindrical magnetic proof mass can be compared to a spherical geometry if the model was 3-dimmensional. The same scenario in 2D would not be a valid comparison because the models would look exactly alike. Tapering the magnet to a trapezoidal shape can also be analyzed. Fig. (5.3) shows a preliminary 2-dimensional model for a trapezoidal proof mass. The goal of optimizing the geometry of the magnetic proof mass would be to mitigate the error associated with cantilever positioning with respect to the conductor.

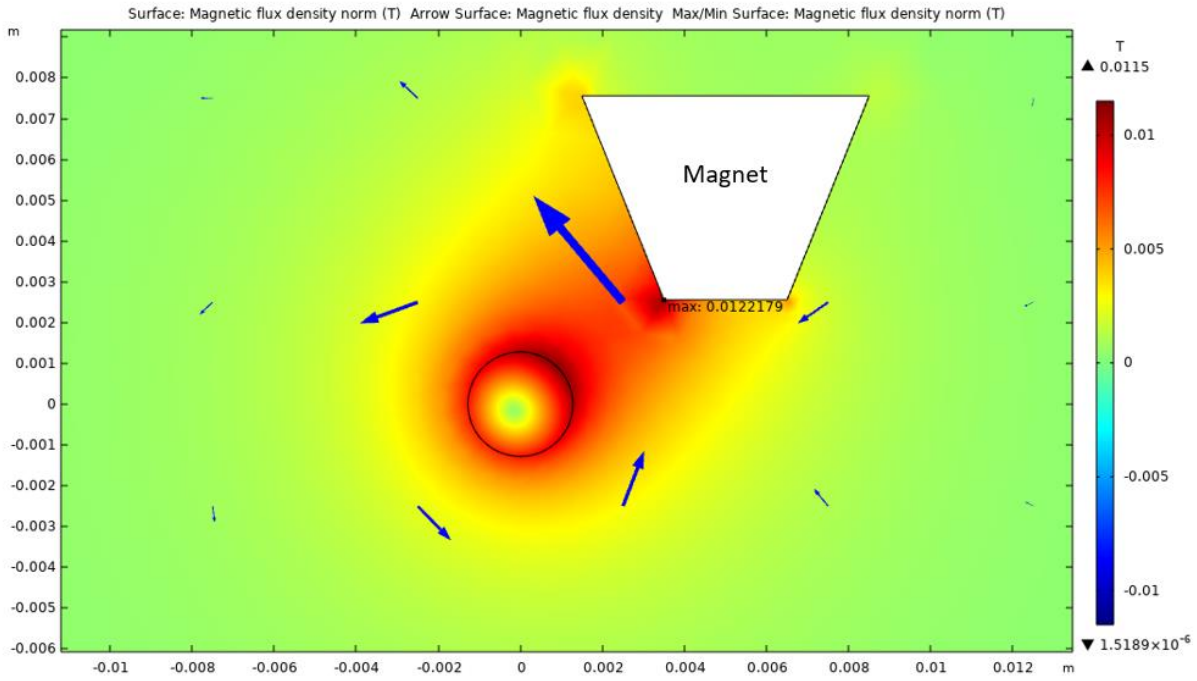

Figure 5. 3: FEM Spatial Optimization with a Trapezoidal Magnet

5.3 Power Storage Circuitry

The sensor proposed in this study must have supporting circuitry to be truly self-sufficient. Although the cantilever itself can produce an electric charge through the

deformation of the piezoelectric layers, this electric energy must be stored. The electricity produced by the cantilever is an AC voltage which cannot be stored. To successfully store the energy the AC voltage must be converted to DC with the use of a full wave rectifier. The charging and discharging of the sensor node must be managed as well. The energy must be stored in a capacitor or battery to be utilized when the signal is ready to be transmitted from the wireless sensor node. There must also be a radio frequency wireless transmitter on the circuit board to send data to the receiving module to be analyzed.

References

Ghasempour, A. (2019). Internet of Things in Smart Grid: Architecture, Applications, Services, Key Technologies, and Challenges. *Inventions*, *4*(1), 22. https://doi.org/10.3390/inventions4010022

Bari, A., Jiang, J., Saad, W., & Jaekel, A. (2014). Challenges in the Smart Grid Applications: An Overview. *International Journal of Distributed Sensor Networks*, *10*(2), 974682. https://doi.org/10.1155/2014/974682

Tuna, G., Gungor, V. C., & Dursun, B. (2017). *Wireless MEMS for smart grids* (pp. 239–258). https://doi.org/10.1016/B978-0-08-100449-4.00011-7

Voljc, B., Lindic, M., & Lapuh, R. (2009). Direct Measurement of AC Current by Measuring the Voltage Drop on the Coaxial Current Shunt. IEEE Transactions on Instrumentation and Measurement, 58(4), 863–867. https://doi.org/10.1109/TIM.2008.2007074

Ripka, P. (2004). Current sensors using magnetic materials. *Journal of Optoelectronics and Advanced Materials*, *6*, 587–592.

Ziegler, S., Woodward, R. C., Iu, H. H.-C., & Borle, L. J. (2009). Current Sensing Techniques: A Review. *IEEE Sensors Journal*, *9*(4), 354–376. https://doi.org/10.1109/JSEN.2009.2013914

Faizal, F., Hafidz, N. s, Florena, F., Maulana, D., Abdurochman, A., Panatarani, C., & Joni, I. M. (2019). Development of high DC-current measurement system using closed loop Hall Effect configuration. IOP Conference Series: Materials Science and Engineering, 550, 012013. https://doi.org/10.1088/1757-899X/550/1/012013

Crescentini, M., Marchesi, M., Romani, A., Tartagni, M., & Traverso, P. A. (2018). A Broadband, On-Chip Sensor Based on Hall Effect for Current Measurements in Smart Power Circuits. IEEE Transactions on Instrumentation and Measurement, 67(6), 1470–1485. https://doi.org/10.1109/TIM.2018.2795248

Cheng, X., Sun, Z., Wang, X., & Liu, S. (2014). Open-loop linear differential current sensor based on dual-mode Hall effect. Measurement, 50, 29–33. https://doi.org/10.1016/j.measurement.2013.12.005

Ouyang, Y., Wang, Z., Zhao, G., Hu, J., Ji, S., He, J., & Wang, S. X. (2019). Current sensors based on GMR effect for smart grid applications. Sensors and Actuators A: Physical, 294, 8–16. https://doi.org/10.1016/j.sna.2019.05.002

Wang, R., Xu, S., Li, W., & Wang, X. (2016). Optical fiber current sensor research: Review and outlook. *Optical and Quantum Electronics*, *48*(9), 442. https://doi.org/10.1007/s11082-016-0719-3

Salazar, R., Serrano, M., & Abdelkefi, A. (2020). Fatigue in piezoelectric ceramic vibrational energy harvesting: A review. *Applied Energy*, *270*, 115161. https://doi.org/10.1016/j.apenergy.2020.115161

Leland, E. S. (n.d.). *A MEMS sensor for AC electric current* [Ph.D., University of California, Berkeley]. Retrieved November 17, 2021, from https://www.proquest.com/docview/516223842/abstract/C5309E16E4D74ACEPQ/1

Ida, N., & Bastos, J. P. A. (1997). *Electromagnetics and Calculation of Fields*. Springer Science & Business Media.

Knoepfel, H. E. (2008). *Magnetic Fields: A Comprehensive Theoretical Treatise for Practical Use*. John Wiley & Sons.

Leland, E. S., Sherman, C. T., Minor, P., White, R. M., & Wright, P. K. (2010). A new MEMS sensor for AC electric current. *2010 IEEE SENSORS*, 1177–1182. https://doi.org/10.1109/ICSENS.2010.5690649

Houlihan, R., Olszewski, O., Waldron, F., O'Neill, M., Mathewson, A., & Jackson, N. (2016). Location Dependence of a MEMS Electromagnetic Transducer with respect to an AC Power Source. *Journal of Physics: Conference Series*, *757*, 012041. https://doi.org/10.1088/1742-6596/757/1/012041

Yeh, P.-C., Chien, T.-H., Hung, M.-S., Chen, C.-P., & Chung, T.-K. (2021). Attachable Magnetic-Piezoelectric Energy-Harvester Powered Wireless Temperature Sensor Nodes for Monitoring of High-Power Electrical Facilities. IEEE Sensors Journal, 21(9), 11140–11154. https://doi.org/10.1109/JSEN.2021.3056275

Lao, S., Chauhan, S., Pollock, T., Schröder, T., Cho, I., & Salehian, A. (2014). Design, Fabrication and Temperature Sensitivity Testing of a Miniature Piezoelectric-Based Sensor for Current Measurements. Actuators, 3(3), 162–181. https://doi.org/10.3390/act3030162

Ghodsi, M., Ziaiefar, H., Mohammadzaheri, M., & Al-Yahmedi, A. (2019). Modeling and characterization of permendur cantilever beam for energy harvesting. Energy, 176, 561–569. https://doi.org/10.1016/j.energy.2019.04.019

Olszewski, O. Z., Houlihan, R., O'Keeffe, R., O'Neill, M., Waldron, F., Mathewson, A., & Jackson, N. (2014). A MEMS Silicon-based Piezoelectric AC Current Sensor. Procedia Engineering, 87, 1457–1460. https://doi.org/10.1016/j.proeng.2014.11.724

R. Houlihan, N. Jackson, A. Mathewson, and O. Z. Olszewski, "A Study on the Spatial Dependence of a MEMS Electromagnetic Transducer," Journal of Microelectromechanical Systems, vol. 28, no. 2, pp. 290–297, Apr. 2019, doi: 10.1109/JMEMS.2018.2887004.

Wang, D. F., Liu, H., Li, X., Li, Y., Xian, W., Kobayashi, T., Itoh, T., & Maeda, R. (2017). Passive MEMS DC Electric Current Sensor: Part I—Theoretical Considerations. *IEEE Sensors Journal*, *17*(5), 1230–1237. https://doi.org/10.1109/JSEN.2016.2644720

Wang, D. F., Liu, H., Li, X., Li, Y., Xian, W., Kobayashi, T., Itoh, T., & Maeda, R. (2017). Passive MEMS DC Electric Current Sensor: Part II–Experimental Verifications. *IEEE Sensors Journal*, *17*(5), 1238–1245. https://doi.org/10.1109/JSEN.2016.2644722

Roundy, S., Otis, B. P., Chee, Y., Rabaey, J. M., & Wright, P. (2003). A 1.9GHz RF Transmit Beacon using Environmentally Scavenged Energy. *Dig. Ieee Int. Symposium on Low Power Elec. and Devices, Seoul, Korea*.

Roundy, S., & Wright, P. K. (2004). A piezoelectric vibration based generator for wireless electronics. *Smart Materials and Structures*, *13*(5), 1131–1142. https://doi.org/10.1088/0964-1726/13/5/018

Andosca, R., McDonald, T., Genova, V., Rosenberg, S., Keating, J., Benedixen, C., & Wu, J. (2012). Experimental and theoretical studies on MEMS piezoelectric vibrational energy harvesters with mass loading. *Sensors and Actuators A: Physical*, *178*, 76–87. https://doi.org/10.1016/j.sna.2012.02.028

Choi, W. J., Jeon, Y., Jeong, J.-H., Sood, R., & Kim, S. G. (2006). Energy harvesting MEMS device based on thin film piezoelectric cantilevers. *Journal of Electroceramics*, *17*(2–4), 543–548. https://doi.org/10.1007/s10832-006-6287-3

Paprotny, I., Xu, Q., Chan, W. W., White, R. M., & Wright, P. K. (2013). Electromechanical Energy Scavenging From Current-Carrying Conductors. *IEEE Sensors Journal*, *13*(1), 190–201. https://doi.org/10.1109/JSEN.2012.2211868

Leland, E. S., White, R. M., & Wright, P. K. (2006). *Energy scavenging power sources for household electrical monitoring*. 4.

Olszewski, O. Z., Houlihan, R., Blake, A., Mathewson, A., & Jackson, N. (2017). Evaluation of Vibrational PiezoMEMS Harvester That Scavenges Energy From a Magnetic Field Surrounding an AC Current-Carrying Wire. *Journal of Microelectromechanical Systems*, *26*(6), 1298–1305. https://doi.org/10.1109/JMEMS.2017.2731400

Yeh, P.-C., Chien, T.-H., Hung, M.-S., Chen, C.-P., & Chung, T.-K. (2021). Attachable Magnetic-Piezoelectric Energy-Harvester Powered Wireless Temperature Sensor Nodes for Monitoring of High-Power Electrical Facilities. *IEEE Sensors Journal*, *21*(9), 11140–11154. https://doi.org/10.1109/JSEN.2021.3056275

Wang, Q., Kim, K.-B., Woo, S.-B., Song, Y., & Sung, T.-H. (2021). A Magneto-Mechanical Piezoelectric Energy Harvester Designed to Scavenge AC Magnetic Field

from Thermal Power Plant with Power-Line Cables. *Energies*, *14*(9), 2387. https://doi.org/10.3390/en14092387

Wang, Q., Kim, K.-B., Woo, S. B., Ko, S. M., Song, Y., & Sung, T. H. (2022). Enhanced electrical performance of spring-supported magneto piezoelectric harvester to achieve 60 Hz under AC magnetic field. *Energy*, *238*, 121693. https://doi.org/10.1016/j.energy.2021.121693

Lao, S., Chauhan, S., Pollock, T., Schröder, T., Cho, I., & Salehian, A. (2014). Design, Fabrication and Temperature Sensitivity Testing of a Miniature Piezoelectric-Based Sensor for Current Measurements. *Actuators*, *3*(3), 162–181. https://doi.org/10.3390/act3030162

Leland, E., Wright, P., & White, R. (2009). A MEMS AC current sensor for residential and commercial electricity end-use monitoring. *Journal of Micromechanics and Microengineering*, *19*, 094018. https://doi.org/10.1088/0960-1317/19/9/094018

Leland, E. S., Sherman, C. T., Minor, P., White, R. M., & Wright, P. K. (2010). A new MEMS sensor for AC electric current. *2010 IEEE SENSORS*, 1177–1182. https://doi.org/10.1109/ICSENS.2010.5690649

Olszewski, O. Z., Houlihan, R., O'Keeffe, R., O'Neill, M., Waldron, F., Mathewson, A., & Jackson, N. (2014). A MEMS Silicon-based Piezoelectric AC Current Sensor. *Procedia Engineering*, *87*, 1457–1460. https://doi.org/10.1016/j.proeng.2014.11.724

Aragonez, O., & Jackson, N. (2021). Spatial Optimization of Piezoelectric Energy Scavenger from Current-Carrying Wire. *2021 IEEE 20th International Conference on Micro and Nanotechnology for Power Generation and Energy Conversion Applications (PowerMEMS)*, 172–175. https://doi.org/10.1109/PowerMEMS54003.2021.9658405

Xian, W., Wang, D. F., Wang, D. F., Kobayashi, T., Maeda, R., & Itoh, T. (2017). A passive position- and pose-free current sensor. *2017 IEEE 12th International Conference on Nano/Micro Engineered and Molecular Systems (NEMS)*, 29–33. https://doi.org/10.1109/NEMS.2017.8016967

Xian, W., & Wang, D. F. (2017). Position and orientation correction scheme for current sensing based on magnetic piezoelectric cantilevers. *Applied Physics Letters*, *110*(14), 143501. https://doi.org/10.1063/1.4979787

Isagawa, K., Wang, D. F., Kobayashi, T., Itoh, T., & Maeda, R. (2011). Development of a MEMS DC electric current sensor applicable to two-wire electrical appliance cord. *2011 6th IEEE International Conference on Nano/Micro Engineered and Molecular Systems*, 932–935. https://doi.org/10.1109/NEMS.2011.6017507

Suzuki, Y., Wang, D., Kobayashi, T., Suwa, Y., Itoh, T., & Maeda, R. (2013, April 16). *Developing MEMS DC Electric Current Sensor for End-use Monitoring of DC Power*

Supply: Part III - Integration with Actuating and Sensing Elements. 2013 Symposium on Design, Test, Integration and Packaging of MEMS/MOEMS, DTIP 2013.

Xu, Q. R., Paprotny, I., Seidel, M., White, R. M., & Wright, P. K. (2013). Stick-On Piezoelectromagnetic AC Current Monitoring of Circuit Breaker Panels. *IEEE Sensors Journal*, *13*(3), 1055–1064. https://doi.org/10.1109/JSEN.2012.2234738